

# Uncovering obscured luminous AGN with WISE

S. Mateos<sup>1\*</sup>, A. Alonso-Herrero<sup>1†</sup>, F. J. Carrera<sup>1</sup>, A. Blain<sup>2</sup>, P. Severgnini<sup>3</sup>  
A. Caccianiga<sup>3</sup>, A. Ruiz<sup>4</sup>

<sup>1</sup> *Instituto de Física de Cantabria (CSIC-Universidad de Cantabria), 39005, Santander, Spain*

<sup>2</sup> *Physics and Astronomy, University of Leicester, University Road, Leicester LE1 7RH, UK*

<sup>3</sup> *INAF-Osservatorio Astronomico di Brera, via Brera 28, 20121 Milano, Italy*

<sup>4</sup> *Inter University Centre for Astronomy and Astrophysics (IUCAA), Post Bag 4, Ganeshkhind, Pune 411 007, India*

Accepted 2013 May 29. Received 2013 May 20; in original form 2013 March 21

## ABSTRACT

Mateos et al. (2012) presented a highly reliable and efficient mid-infrared (MIR) colour-based selection technique for luminous active galactic nuclei (AGN) using the *Wide-field Infrared Survey Explorer* (WISE) survey. Here we evaluate the effectiveness of this technique to identify obscured AGN missed in X-ray surveys. To do so we study the WISE properties of AGN independently selected in hard X-ray and optical surveys. We use the largest catalogue of 887 [O III]  $\lambda$ 5007-selected type 2 quasars (QSO2s) at  $z \lesssim 0.83$  in the literature from the Sloan Digital Sky Survey, and the 258 hard ( $>4.5$  keV) X-ray-selected AGN from the Bright Ultrahard *XMM-Newton* Survey (BUXS). The fraction of SDSS QSO2s in our infrared AGN selection region (wedge) increases with the AGN luminosity, reaching  $66.1^{+4.5}_{-4.7}\%$  at the highest [O III] luminosities in the sample. This fraction is substantially lower than for the BUXS type 1 AGN ( $96.1^{+3.0}_{-6.3}\%$ ), but consistent, within the uncertainties, with that for the BUXS type 2 AGN ( $75.0^{+14.1}_{-19.1}\%$ ) with the same luminosity. The SDSS QSO2s appear to reside in more luminous (massive) hosts than the BUXS AGN, due to the tight magnitude limits applied in the SDSS spectroscopic target selection. Since host galaxy dilution can reduce substantially the effectiveness of MIR-based techniques, this may explain the lower fraction of SDSS QSO2s in the WISE AGN wedge. The fraction of SDSS QSO2s identified as Compton-thick candidates that fall in the wedge is consistent with the fraction of all SDSS QSO2s in that zone. At the AGN luminosities involved in the comparison, Compton-thick and Compton-thin SDSS QSO2s have similar WISE colour distributions. We conclude that at high luminosities and  $z \lesssim 1$  our MIR technique is very effective at identifying both Compton-thin and Compton-thick AGN.

**Key words:** galaxies: active-quasars: general-infrared: galaxies

## 1 INTRODUCTION

Providing a complete census of the obscured active galactic nuclei (AGN) population is crucial to fully understand the cosmological growth of supermassive black holes (SMBH) and to reveal the physical nature of the SMBH-galaxy co-evolution (e.g. Magorrian et al. 1998; Tremaine et al. 2002). A population of heavily obscured AGN at cosmological distances is required to explain the shape of the Cosmic X-ray background spectrum as shown by the latest AGN population synthesis models (Gilli, Comastri, & Hasinger 2007; Treister, Urry, & Virani 2009; Ballantyne et al. 2011; Shi et al. 2012). Deep hard X-

ray surveys with *XMM-Newton* and *Chandra* (up to  $\sim 10$  keV) have provided the most complete and unbiased samples of AGN spanning a broad range of luminosities and redshifts (e.g. Mainieri et al. 2002; Alexander et al. 2003; Brandt & Hasinger 2005; Mateos et al. 2005; Tozzi et al. 2006; Brandt & Alexander 2010; Xue et al. 2011). However, there is strong observational evidence that even the deepest X-ray surveys conducted to date are incomplete for AGN with heavy obscuration (line of sight neutral Hydrogen column densities  $N_{\text{H}} > 10^{23} \text{ cm}^{-2}$ ) and they miss many of the objects with Compton-thick ( $N_{\text{H}} \gtrsim 1.5 \times 10^{24} \text{ cm}^{-2}$ ) obscuration (Della Ceca et al. 2008; Comastri et al. 2011; Iwasawa et al. 2012). Compton-thick AGN could represent a fraction as large as  $\sim 20$ -30% of the entire AGN population (e.g. Worsley et al. 2005; Burlon et al. 2011).

In this context surveys at mid-infrared (MIR) wave-

\*E-mail: mateos@ifca.unican.es

†Augusto G. Linares Senior Research Fellow

lengths ( $\gtrsim 5\mu\text{m}$ ) are much less affected by extinction. Since most of the absorbed AGN energy is re-emitted in the MIR, surveys at these wavelengths can potentially recover the elusive obscured accretion missed by X-ray surveys (e.g. Lacy et al. 2004; Stern et al. 2005; Alonso-Herrero et al. 2006; Fiore et al. 2008; Georgantopoulos et al. 2008; Donley et al. 2012; Severgnini, Caccianiga, & Della Ceca 2012).

The *Wide-field Infrared Survey Explorer* (WISE; Wright et al. 2010) has completed the first sensitive survey of the entire sky at 3.4, 4.6, 12, and  $22\mu\text{m}$  providing an unprecedented dataset at MIR wavelengths. AGN population studies with WISE are starting to fill the gap between local/deep MIR surveys with *IRAS/Spitzer* in regions of the parameter space poorly sampled. MIR selection techniques rely on identifying objects with red power-law SEDs, the characteristic signature of hot dust heated by the intense radiation field of the AGN (Alonso-Herrero et al. 2006). Several works in the literature have already demonstrated that using WISE colours alone it is possible to separate stars and normal/star-forming galaxies from luminous AGN (Assef et al. 2012; Mateos et al. 2012; Stern et al. 2012; Yan et al. 2012).

In Mateos et al. (2012, hereafter M12) we presented an MIR colour-based selection of luminous AGN candidates using the 3.4, 4.6, and  $12\mu\text{m}$  bands of WISE. The reliability and effectiveness of the technique were evaluated using the 258 hard ( $>4.5\text{ keV}$ ) X-ray-selected AGN from the Bright Ultrahard *XMM-Newton* Survey (BUXS; M12). Surveys such as BUXS are the most efficient and complete way of tracing the accretion phenomenon in the Universe at column densities approaching the Compton-thick limit (e.g. Caccianiga et al. 2004; Della Ceca et al. 2008). We demonstrated that our technique, aimed to identify objects with red MIR spectral energy distributions (SEDs), is highly reliable and very effective for the detection of (X-ray) luminous AGN. At  $L_{2-10\text{ keV}}$  in the range  $10^{44}\text{--}10^{45}\text{ erg s}^{-1}$ ,  $96.1^{+3.0}_{-6.3}\%$  and  $75.0^{+14.1}_{-19.1}\%$  of the BUXS type 1 and type 2 AGN meet the selection, respectively. Interestingly, we found that hard X-ray surveys preferentially miss the WISE AGN candidates with the reddest MIR colours. Objects such as these are the best candidates to account, at least in part, for the obscured/absorbed luminous AGN largely missed by X-ray surveys. The hard X-ray signal obtained from stacking analyses of X-ray non-detected infrared AGN candidates suggests that in these objects the nuclear emission is obscured by heavy/Compton-thick material (e.g. Donley et al. 2012).

However, there is still little knowledge on the nature and properties of the AGN populations identified with WISE and, more importantly, the impact of heavy nuclear obscuration on the effectiveness of WISE selection techniques, even at high luminosities. To get insight into these issues we have evaluated the effectiveness of our MIR selection technique for the largest catalogue of 887 type 2 quasars (QSO2s) at  $z \lesssim 0.83$  in the literature from the Sloan Digital Sky Survey (SDSS; Reyes et al. 2008). The objects were selected based on their high [O III]  $\lambda 5007$  line luminosities,  $L_{[\text{O III}]}\geq 10^{8.3}L_{\odot}$ . As [O III] fluxes are largely unaffected by AGN nuclear absorption/obscuration, this sample of luminous QSO2s should not be biased against heavily obscured objects. Therefore, we can use this dataset to evaluate whether AGN selection techniques with WISE are able

to identify luminous obscured AGN at  $z \lesssim 1$  missed in X-ray surveys. Furthermore, to get insight into the nature of the WISE AGN candidates, especially those objects with red infrared SEDs not detected in X-rays, we studied the properties (infrared colour distributions and median rest-frame UV-to-MIR SEDs) of the AGN independently selected in X-ray and optical surveys using the data from BUXS and the SDSS QSO2 catalogue.

This paper is organized as follows. Section 2 briefly summarizes the data sets. In Section 3 we determine the effectiveness of our infrared selection technique for the full sample of SDSS QSO2s and for those objects identified in the literature as Compton-thick candidates, and we compare it with the results obtained for the X-ray selected AGN in the BUXS survey. In Section 4 we compare the distributions of WISE colours for the different classes of AGN and we compute and present the properties of their median SEDs. In Section 5 we discuss the main results of our analysis. The results are summarized in Section 6. Throughout this paper errors are 90% confidence for a single parameter ( $\Delta\chi^2=2.71$ ) unless otherwise stated. We estimated the most probable value for the fractions using a Bayesian approach and the binomial distribution from Wall & Jenkins (2008) and the quoted errors are the narrowest interval that includes the mode and encompasses 90% of the probability. The terms “red” and “blue” refer to increasing or decreasing fluxes in  $\nu f_{\nu}$  at longer wavelengths, respectively. We adopt the concordance cosmology,  $\Omega_M = 0.3$ ,  $\Omega_{\Lambda} = 0.7$ , and  $H_0 = 70\text{ km s}^{-1}\text{ Mpc}^{-1}$ .

## 2 SAMPLE DESCRIPTION

### 2.1 SDSS catalogue of [O III] $\lambda 5007$ QSO2s

Here we use the largest catalogue of type 2 quasars in the literature derived from the SDSS (Stoughton et al. 2002; York et al. 2000) spectroscopic database (Reyes et al. 2008; hereafter R08). The catalogue includes objects with UV/optical narrow emission lines only and with line ratios characteristic of non-stellar ionizing radiation. As shown by Villar et al. (2008), standard AGN photoionization models can reproduce successfully the main emission-line ratio diagnostic diagrams at least at high [O III] luminosities. The R08 catalogue includes only objects with  $L_{[\text{O III}]}\geq 10^{8.3}L_{\odot}$  and  $z < 0.83$  to ensure that the [O III]  $\lambda 5007$  line is present in the SDSS spectra. The R08 catalogue includes both Gaussian and non-parametric [O III] line measurements, the latter (used to define the luminosity cut) being systematically larger by 5% on average. In this paper  $L_{[\text{O III}]}$  refers to luminosities estimated from Gaussian fits. The catalogue contains 887 type 2 quasars detected over a survey area of  $\approx 6293\text{ deg}^2$ . From now on, we will refer to this source sample as the SDSS QSO2s.

The objects in R08 were selected independently of their X-ray properties with a selection that should be unaffected by nuclear obscuration. Only a small subset of the SDSS QSO2s have X-ray information, which is necessary to directly measure the absorption along the line of sight. Detailed analyses of their X-ray properties suggest that, at least at the highest [O III] luminosities, most SDSS QSO2s are heavily absorbed and an important fraction

might be Compton-thick (Ptak et al. 2006; LaMassa et al. 2009; Vignali et al. 2010; Jia et al. 2012). Similar results are found for [O III]  $\lambda 5007$ -selected AGN at lower luminosities (Goulding et al. 2011). Thus, we can confidently use the SDSS QSO2 catalogue to evaluate the effectiveness of the infrared AGN wedge to select luminous absorbed AGN at  $z \lesssim 1$  in a way that is relatively free from the potential selection effects of X-ray absorption.

We caution however, that the objects in the R08 catalogue were selected from different SDSS spectroscopic target selection algorithms which implies that the selection function is different across the luminosity- $z$  range of the sample. At  $z \leq 0.3$  (and lower [O III] luminosities) most SDSS QSO2s were targeted by the Main Galaxy algorithm (based on optical morphology i.e. resolved objects) while at  $z > 0.3$  (and higher [O III] luminosities) the SDSS QSO2s were mainly targeted by the Low- $z$  and High- $z$  QSO (non-stellar colour selection) and Serendipity FIRST (radio properties) algorithms (see Fig. 3 in R08). We will discuss how this property of the SDSS QSO2 catalogue might affect our results. A summary of the SDSS spectroscopic target selection algorithms is given in R08 while for more detailed information see Richards et al. (2002) and Strauss et al. (2002).

## 2.2 The Bright Ultra-hard *XMM-Newton* Survey

BUXS is a complete flux-limited sample of bright ( $f_{4.5-10 \text{ keV}} > 6 \times 10^{-14} \text{ erg s}^{-1} \text{ cm}^{-2}$ ) “ultra-hard” (4.5-10 keV) X-ray selected sources detected over a total sky area of 44.43 deg<sup>2</sup>. BUXS is based on a subset of 381 high galactic latitude ( $|b| > 20 \text{ deg}$ ) observations from the second *XMM-Newton* serendipitous source catalogue (2XMM; Watson et al. 2009). These observations, with effective exposure times in the range 10-100 ks, were used to derive high precision X-ray extragalactic source count distributions at intermediate fluxes (Mateos et al. 2008). At the time of writing the spectroscopic identification completeness is 97.3%. Of the 258 BUXS sources, 145 objects (56.2%) are identified as type 1 AGN (showing UV/optical emission line velocity widths  $\geq 1500 \text{ km s}^{-1}$ ) and 106 (41.1%) as type 2 AGN (showing UV/optical emission line velocity widths  $< 1500 \text{ km s}^{-1}$  or a galaxy spectrum with no emission lines) while 7 sources (2.7%) remain unidentified. BUXS covers 4 decades in X-ray luminosity ( $\sim 10^{42} - 10^{46} \text{ erg s}^{-1}$ ) and extends up to  $z \sim 2$ . X-ray luminosities are computed in the “standard” 2-10 keV rest-frame energy band. They were derived from a detailed analysis of the X-ray spectra of the objects and they are corrected for intrinsic absorption.

## 2.3 WISE infrared data

We use here the most recent publicly available All-Sky Data Release that covers  $>99\%$  of the sky (March 2012; Cutri et al. 2012<sup>1</sup>). WISE estimated  $5\sigma$  point source sensitivities are better than 0.07, 0.1, 0.9, and 5.4 mJy at 3.4, 4.6, 12, and 22  $\mu\text{m}$ , respectively, although the depth increases with the ecliptic latitude (Jarrett et al. 2011). The angular resolution is (FWHM) 6.1”, 6.4”, 6.5”, and 12” in

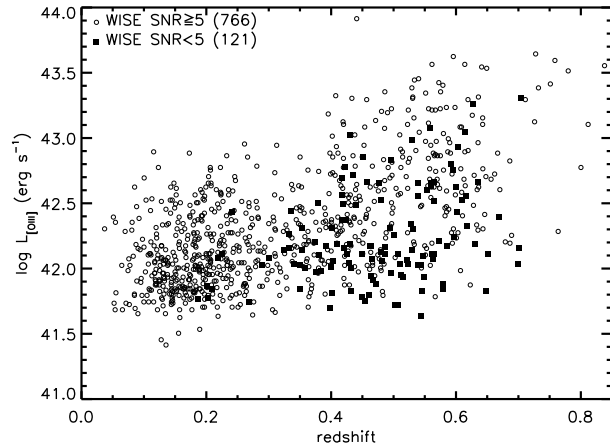


**Figure 1.** Distribution of the [O III]  $\lambda 5007$  line luminosity (in logarithmic units) versus  $z$  for the SDSS QSO2s in the R08 catalogue. Objects detected with  $\text{SNR} \geq 5$  in the three shorter wavelength bands of WISE are indicated with open circles. Filled squares indicate the objects without WISE counterparts and those with  $\text{SNR} < 5$  in any of the three shorter wavelength bands of WISE (17 and 104, respectively).

the four WISE bands, respectively. The astrometric precision for sources with signal-to-noise ratio (hereafter SNR)  $\text{SNR} > 20$  in at least one WISE band is better than 0.15” (Wright et al. 2010).

We computed flux densities using profile fitting photometry and the magnitude zero points of the Vega system that correspond to a power-law spectrum ( $f_\nu \propto \nu^\alpha$ ) with spectral index  $\alpha = -1$  (Wright et al. 2010):  $F_\nu$  (iso) = 309.124 Jy, 171.641 Jy, 30.988 Jy, and 8.346 Jy for 3.4, 4.6, 12, and 22  $\mu\text{m}$ , respectively. Using the flux correction factors that correspond to constant power-law spectra the difference in the computed flux densities would be less than 0.2% at 3.4, 4.6, and 22  $\mu\text{m}$  and  $\sim 2\%$  at 12  $\mu\text{m}$ . We added a 1.5% uncertainty to the catalogued flux errors in all bands to account for the overall systematic uncertainty from the Vega spectrum in the flux zero-points. To account for the existing discrepancy between the red and blue calibrators used for the conversion from magnitudes to Janskys an additional 10% uncertainty was added to the 12  $\mu\text{m}$  and 22  $\mu\text{m}$  fluxes (Wright et al. 2010). Throughout this paper we use monochromatic MIR flux densities ( $f_\nu$ ) in Janskys, unless otherwise specified.

### 2.3.1 Detection of SDSS QSO2s with WISE

We cross-matched the SDSS QSO2 and the all-sky WISE catalogues using a search radius of 2”. All but 17 objects have MIR counterparts. We checked that for two of these sources a blend of two WISE objects prevents us from identifying a unique MIR counterpart. The remaining 15 sources are not detected with WISE even if we increase the search radius.

Since in this paper we use the WISE AGN selection technique from M12 (see Sec. 3.1), which identifies AGN candidates among WISE objects detected with  $\text{SNR} \geq 5$  at all 3.4, 4.6, and 12  $\mu\text{m}$ , in the following we use the same

<sup>1</sup> <http://wise2.ipac.caltech.edu/docs/release/allsky/>

**Table 1.** Summary of the properties of the different source samples used in this study.

Sample	$N_{\text{tot}}$	$N_{\text{SNR}\geq 5}$	$N_{\text{wedge}}$	$\Omega$ (deg <sup>2</sup> )	$f_{12\mu\text{m}}$ (mJy)	$z$	$\log(L_{2-10\text{ keV}})$ (erg/s)
(1)	(2)	(3)	(4)	(5)	(6)	(7)	(8)
SDSS QSO2s	887	766	408	6293	3.21	0.26	43.88
BUXS type 1	145	114	105	44.43	1.32	0.64	44.34
BUXS type 2	106	81	38	44.43	1.71	0.23	43.38
BUXS WISE	448909	25206	2755	44.43	0.82	-	-
BUXS WISE+X	6377	1659	1062	44.43	0.96	-	-

Column 1: Source sample; column 2: total number of objects in sample; column 3: number of objects detected with  $\text{SNR}\geq 5$  in all the first three bands of WISE; column 4: number of objects in the infrared AGN wedge; column 5: solid angle of the survey; columns 6, 7 and 8: median  $12\mu\text{m}$  flux,  $z$  and 2-10 keV luminosity for those objects with detection  $\text{SNR}\geq 5$  in all the first three bands of WISE. For comparison, the median  $12\mu\text{m}$  flux of the WISE AGN candidates in the infrared wedge not detected in X-rays is 0.75 mJy. For the SDSS QSO2s the luminosities were derived using the empirical relation between hard X-ray emission and [O III]  $\lambda 5007$  luminosity from Jin et al. (2012) (see Sec. 3.3). For the BUXS AGN, the luminosities were computed from the analysis of their X-ray spectra and they are corrected for Galactic and intrinsic absorption.

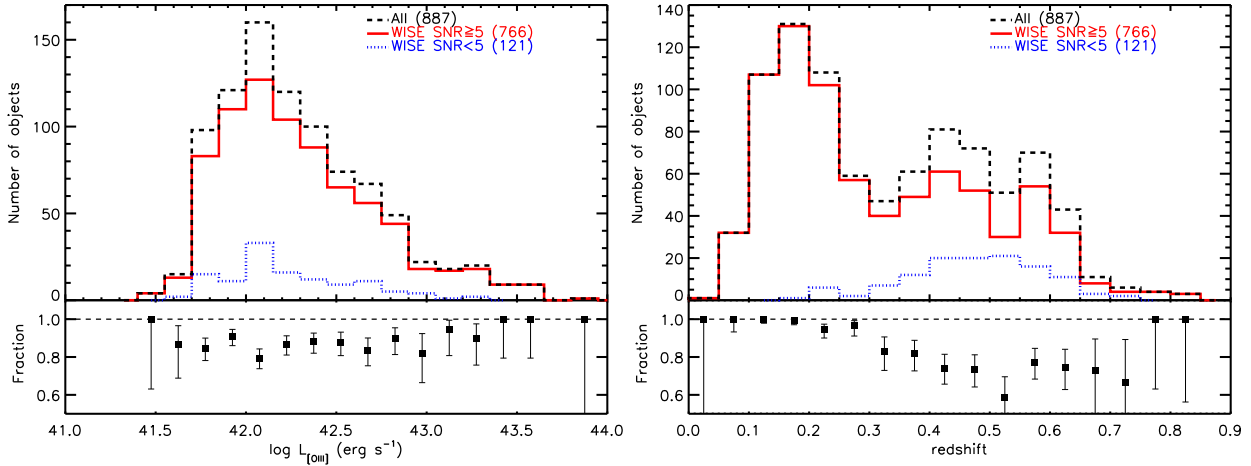


**Figure 2.** [O III]  $\lambda 5007$  luminosity (in logarithmic units, left) and  $z$  (right) distributions of the SDSS QSO2s in R08. We show the distributions for the full sample (dashed), those objects detected with  $\text{SNR}\geq 5$  at all 3.4, 4.6, and  $12\mu\text{m}$  (solid), and those without WISE counterparts or with  $\text{SNR}< 5$  in any of the three shorter wavelength bands of WISE (17 and 104, respectively). The plots at the bottom indicate the fraction of SDSS QSO2s detected with  $\text{SNR}\geq 5$  at all 3.4, 4.6, and  $12\mu\text{m}$  as a function of [O III]  $\lambda 5007$  luminosity (left) and  $z$  (right), respectively.

infrared detection criteria. Table 1 summarizes the main properties of the SDSS QSO2s selected for this study as well as those of the BUXS AGN (see Sec. 2.3.2). Fig. 1 shows the [O III]  $\lambda 5007$  line luminosity versus  $z$  distribution for the SDSS QSO2s with  $\text{SNR}\geq 5$  in all three (3.4, 4.6, and  $12\mu\text{m}$ ) bands (766) and without detection or  $\text{SNR}< 5$  in any of those bands (121, of which 17 do not have a WISE counterpart). Fig. 2 compares their [O III]  $\lambda 5007$  luminosity (left) and  $z$  (right) distributions and indicates the fraction of SDSS QSO2s detected in all the first three bands of WISE as a function of luminosity and  $z$  (bottom panels). As Fig. 1 shows, we lose preferentially the least luminous (on the basis of their [O III]  $\lambda 5007$  line luminosity) SDSS QSO2s at  $z>0.3$ . Still, the detection fraction is high and remains above  $\sim 70\%$  over most of the luminosity- $z$  range. This ensures that our WISE three-band detection and SNR requirements will not bias any of the results of the paper.

### 2.3.2 Matching WISE with BUXS

To reliably identify the WISE counterparts of the BUXS AGN we used the cross-matching algorithm of Pineau et al. (2011), which is based on the classical likelihood ratio. Full details on the cross-correlation are given in M12. In total 255 out of 258 objects (98.8%) have WISE counterparts (i.e. detection with  $\text{SNR}\geq 5$  in at least one band). The number of such objects detected with  $\text{SNR}\geq 5$  at all 3.4, 4.6, and  $12\mu\text{m}$ , is 114 out of 145 (78.6%) type 1 AGN and 81 out of 106 (76.4%) type 2 AGN (see Table 1).

To get insight into the nature of the WISE objects identified as AGN, in M12 we studied the properties (infrared colours) of all catalogued WISE sources in the BUXS survey area detected in all the first three bands of WISE (25206 objects), and of those sources with X-ray detection at 2-10 keV energies down to the full depth of the X-ray data (1659 objects). One of the most interesting results from the M12 study is that the fraction of WISE objects identified as AGN from X-rays decreases substantially at the reddest

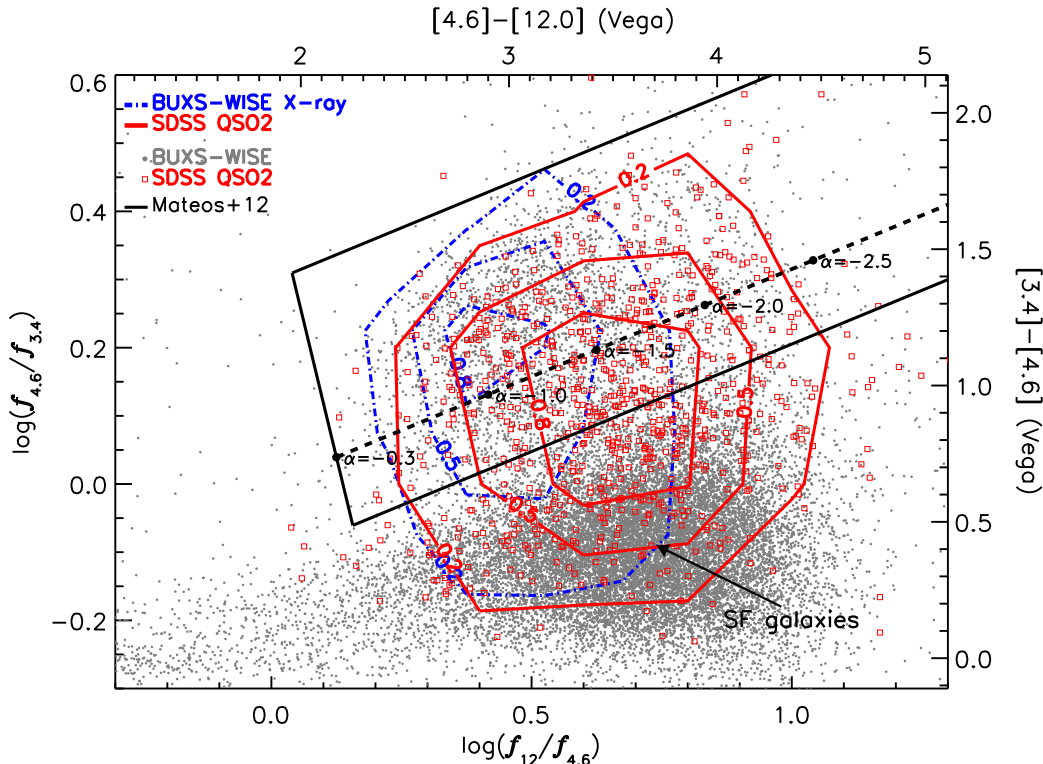


**Figure 3.** WISE MIR colours for sources detected with  $\text{SNR} \geq 5$  at all 3.4, 4.6, and  $12 \mu\text{m}$ . Filled circles are all the WISE sources in the BUXS survey area, i.e., not applying any of the X-ray selection criteria that define the BUXS AGN sample (see Sec. 2.3.2 and Table 1). The SDSS QSO2s in R08 are shown as open squares. The M12 infrared AGN wedge and power-law locus (and the values for different spectral index) are the thick solid and dashed lines, respectively. The solid and dotted-dashed contours indicate the densities (normalized to the peak value) of the SDSS QSO2s and all the WISE sources in the BUXS area detected at 2–10 keV energies down to the full depth of the X-ray data, respectively.

MIR colours (see Fig. 2 in M12). Objects of this sort could account for part of the population of absorbed AGN largely missed by hard X-ray surveys. Currently only a small fraction of the WISE AGN candidates not detected in X-rays in the BUXS area have optical spectroscopic identifications (<9%), almost all from SDSS. Clearly these identifications are biased towards blue type 1 AGN and therefore they are not representative of the underlying AGN population. Thus, to get more insight into the nature of the WISE AGN, in this work we compare their infrared colours with those of the BUXS type 1 and type 2 AGN and the SDSS QSO2s.

Table 1 gives a summary of the properties of the different source samples derived from the BUXS survey that we use in this study.

### 3 WISE AGN SELECTION FOR SDSS QSO2

#### 3.1 Our infrared AGN selection technique

In M12 we used the data from the BUXS survey to define an MIR colour selection of luminous AGN using the three shorter wavelength bands of WISE (hereafter infrared AGN wedge). The technique, that properly takes into account the errors in the photometry, can robustly identify with high

completeness X-ray luminous AGN down to a  $\text{SNR}=5$  significance of detection at all 3.4, 4.6, and  $12 \mu\text{m}$ . At  $L_{2-10 \text{ keV}}$  from  $10^{44}$  to  $10^{45} \text{ erg s}^{-1}$ ,  $96.1^{+3.0}_{-6.3}\%$  and  $75.0^{+14.1}_{-19.1}\%$  of the BUXS type 1 and type 2 AGN meet the selection, respectively. The number of WISE objects in the BUXS area in the infrared AGN wedge (both with and without X-ray detection) are reported in Table 1. We note that the overlap of the BUXS and SDSS QSO2 samples is very small as there are only three sources in common between the SDSS QSO2s and the WISE sources in BUXS in the infrared AGN wedge.

#### 3.2 Effectiveness of the WISE selection as a function of [O III] luminosity

The distribution of WISE infrared colours of the SDSS QSO2s is shown in Fig. 3 (open squares and thick solid line contours). Fig. 3 also shows the infrared AGN wedge defined in M12 and the power-law locus for different values of the spectral index<sup>2</sup> with solid and dashed lines, respectively. For comparison we show the colours of the WISE sources detected in the BUXS fields (small filled circles) and of those

<sup>2</sup> Power-law spectrum  $f_\nu \propto \nu^\alpha$  with spectral index  $\alpha$

objects with detection at 2-10 keV X-ray energies (dotted-dashed contours). As in M12 we are assuming that an X-ray detection  $>2$  keV is a good tracer of unabsorbed and mildly absorbed AGN activity.

From Fig. 3 it is clear that a substantial fraction of the SDSS QSO2s have infrared colours typical of low  $z$  star-forming galaxies (horizontal sequence in the lower-right part of the diagram). Indeed, out of the 766 SDSS QSO2s with detection in the three shortest wavelength bands of WISE only 408 ( $53.3 \pm 3\%$ ) fall in the infrared AGN wedge. The remainder are in a continuous extension to bluer  $\log(f_{4.6}/f_{3.4})$  colours, presumably due to increasing amounts of contributed flux from starlight in the AGN host galaxy. At low luminosities and for objects with large extinction at rest-frame infrared wavelengths, the emission from the host galaxy contaminates the observed flux preventing the detection of the AGN signatures with infrared colour and power-law based selection techniques. In particular, the shortest wavelengths will be the most contaminated ones producing a shift towards the lowest-right part of the diagram. Thus, the effectiveness of any MIR selection strongly depends on the AGN luminosity (e.g. Alonso-Herrero et al. 2006; Eckart et al. 2010; Donley et al. 2012; Mateos et al. 2012). Fig. 4 shows the dependence on luminosity of the fraction of SDSS QSO2s in the infrared AGN wedge. The fractions were computed in bins of 0.2 in luminosity and are reported in Table 2. The infrared selection is, as expected, a strong function of the AGN luminosity.

There is a decrease in the fraction of SDSS QSO2s in the infrared AGN wedge at the highest [O III] luminosities. We caution however, that at these luminosities and  $z$  the SDSS QSO2 catalogue is far from being complete or representative of the QSO2 population (see Fig. 1). Furthermore, as noted in Sec. 2.1 careful attention must be paid when comparing the results for objects from different SDSS spectroscopic target selections. In Table 2 we compare the fractions of SDSS QSO2s in the infrared AGN wedge for objects at  $z \leq 0.3$  and  $z > 0.3$ , respectively. Although the values are consistent within the uncertainties, at the highest luminosities they are systematically lower for the SDSS QSO2s at  $z > 0.3$ . This effect is most likely associated with the different selection functions at  $z \leq 0.3$  and  $z > 0.3$ . For example, at  $z > 0.3$  most sources were targeted by the QSO algorithms (see Sec. 2.1) that pre-select objects with non-stellar colours (blue) in the *ugriz* broad-band photometry. It is not unexpected that their blue optical SEDs will extend to the near-infrared, and hence these objects would easily be missed by infrared selection techniques targeting AGN with red infrared SEDs. However, we cannot rule out that the apparent decrease in effectiveness is due in part to the k-correction (i.e. the host galaxy emission contaminates the WISE fluxes at the shortest wavelengths).

### 3.3 Comparison with an X-ray selected sample

Most SDSS QSO2s in R08 have not been observed in X-rays. Hence, to compare with the results for the AGN in BUXS (overplotted in Fig. 4) we derived intrinsic 2-10 keV rest-frame luminosities using the empirical relation between hard X-ray emission and [O III]  $\lambda 5007$  luminosity for type 1 AGN from Jin et al. (2012) (hereafter J12),

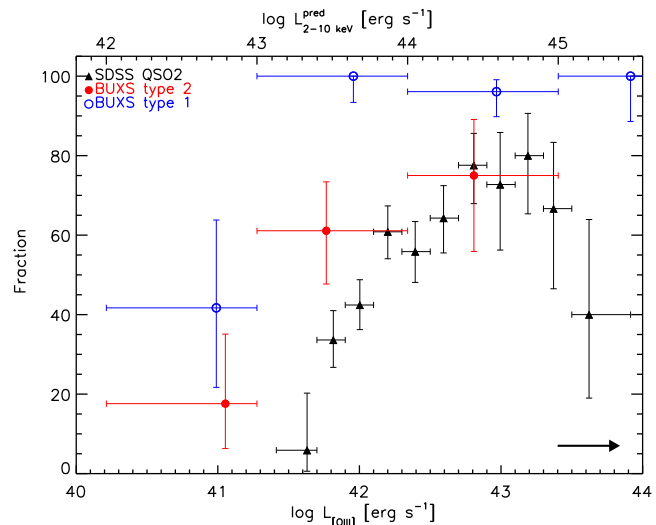


**Figure 4.** Fraction of SDSS QSO2s in the infrared AGN wedge as a function of the [O III]  $\lambda 5007$  line luminosity (in logarithmic units; triangles). The symbols indicate the mean luminosity of the sources in the bin. The top axis indicates the predicted rest-frame 2-10 keV luminosities derived from the empirical relation between the X-ray and [O III]  $\lambda 5007$  luminosities of J12 (see Sec. 3.3). The results obtained for the BUXS type 1 and type 2 AGN are indicated with open and filled circles, respectively. For the BUXS AGN the X-ray luminosities were derived from the modeling of their X-ray spectra and are corrected for intrinsic absorption. The horizontal arrow at the bottom right shows the amplitude of the median extinction correction to the [O III] line luminosities (see Sec. 3.3).

$$\log(L_{2-10 \text{ keV}}) = (0.94 \pm 0.05) \times \log(L_{[\text{OIII}]}) + (4.20 \pm 2.26) \quad (1)$$

Here we are assuming that the above relation is the same for both type 1 and type 2 AGN, and that observed differences are mainly due to obscuration/absorption (e.g. Heckman et al. 2005). J12 used a large sample of SDSS type 1 AGN with high quality *XMM-Newton* spectroscopy, low reddening and unobscured X-ray emission. This allowed to constrain better the empirical relation compared to previous works (e.g. Heckman et al. 2005; Lamastra et al. 2009; Trouille & Barger 2010; Jin et al. 2012). Using the J12 relation we are also accounting for systematic differences in the  $L_{[\text{OIII}]} / L_{2-10 \text{ keV}}$  distributions measured for X-ray and optically selected AGN (e.g. Netzer et al. 2006).

We have not corrected for extinction the [O III]  $\lambda 5007$  luminosities, hence predicted X-ray luminosities will be somewhat higher for some SDSS QSO2s. For many objects, the SDSS spectral coverage does not reach the rest-frame wavelengths of the  $H\alpha$  line and the SNR of higher order Balmer lines is not sufficient to reliably measure line luminosities. Furthermore, extinctions based on the  $H\alpha/H\beta$  and  $H\beta/H\gamma$  ratios are inconsistent with standard reddening laws (see R08). R08 derived a median Balmer line ratio  $H\alpha/H\beta = 4.25$  for 44 SDSS QSO2s with  $L_{[\text{OIII}]} > 3.8 \times 10^{42} \text{ erg s}^{-1}$  at  $z < 0.4$ . Using the Bassani et al. (1999) relation to derive extinction-corrected luminosities,  $\log(L_{[\text{OIII}]}) = \log(L_{[\text{OIII}]}) + 0.44$ , for an intrinsic Balmer decrement of 3.0. Assuming that all SDSS QSO2s suffer the same level of extinction, such uncertainty level (indicated by the horizontal arrow at the

**Table 2.** Luminosity and  $z$  dependence of the fraction of SDSS QSO2s in the infrared AGN wedge.

$\log(L_{[\text{OIII}]})$ (1)	$N_{\text{tot}}$ (2)	$f_{\text{tot}}$ (3)	$N_{z \leq 0.3}$ (4)	$f_{z \leq 0.3}$ (5)	$N_{z > 0.3}$ (6)	$f_{z > 0.3}$ (7)
[41.4–41.7]	17	$5.9^{+14.4}_{-5.3}$	15	$6.7^{+15.9}_{-6.0}$	2	$0.0^{+53.6}_{-18.0}$
[41.7–41.9]	116	$33.6^{+7.4}_{-6.9}$	101	$32.7^{+7.9}_{-7.3}$	15	$40.0^{+20.1}_{-13.2}$
[41.9–42.1]	165	$42.4^{+6.3}_{-6.2}$	129	$40.3^{+7.2}_{-6.9}$	36	$50.0^{+13.2}_{-13.2}$
[42.1–42.3]	143	$60.8^{+6.5}_{-6.8}$	83	$66.3^{+8.0}_{-8.7}$	60	$53.3^{+10.2}_{-10.4}$
[42.3–42.5]	111	$55.9^{+7.6}_{-7.7}$	54	$63.0^{+10.1}_{-11.0}$	57	$49.1^{+10.7}_{-10.6}$
[42.5–42.7]	84	$64.3^{+8.2}_{-8.8}$	36	$77.8^{+9.7}_{-12.4}$	48	$54.2^{+11.3}_{-11.6}$
[42.7–42.9]	58	$77.6^{+8.0}_{-9.7}$	12	$91.7^{+7.4}_{-18.9}$	47	$74.5^{+9.3}_{-11.1}$
[42.9–43.1]	22	$72.7^{+13.1}_{-16.5}$	-	-	21	$71.4^{+13.6}_{-17.0}$
[43.1–43.3]	25	$80.0^{+10.6}_{-14.6}$	-	-	25	$80.0^{+10.6}_{-14.6}$
[43.3–43.5]	15	$66.7^{+16.7}_{-20.2}$	-	-	15	$66.7^{+16.7}_{-20.2}$
[43.5–44.0]	10	$40.0^{+23.9}_{-21.0}$	-	-	10	$40.0^{+23.9}_{-21.0}$
Total	766	$53.3^{+3.0}_{-3.0}$	430	$49.8^{+4.0}_{-4.0}$	336	$57.7^{+4.4}_{-4.4}$

Column 1: X-ray luminosity range of the bin in units of  $\text{erg s}^{-1}$  (logarithmic units); column 2: number of SDSS QSO2s; column 3: fraction of SDSS QSO2s in the infrared AGN wedge; column 4: number of SDSS QSO2s at  $z \leq 0.3$ ; column 5: fraction of SDSS QSO2s at  $z \leq 0.3$  in the infrared AGN wedge; column 6: number of SDSS QSO2s at  $z > 0.3$ ; column 7: fraction of SDSS QSO2s at  $z > 0.3$  in the infrared AGN wedge.

**Table 3.** Comparison of the effectiveness of the infrared AGN wedge for the BUXS AGN and SDSS QSO2s.

$\log(L_{2-10 \text{ keV}})$ (1)	$f_{\text{type 1}}$ (2)	$f_{\text{type 2}}$ (3)	$f_{\text{QSO2s}}$ (4)	$f_{\text{QSO2s}}^{\text{corr}}$ (5)
[43–44]	$100_{-6.6}$	$61.1^{+12.3}_{-13.4}$	$45.5^{+3.8}_{-3.8}$	$30.1^{+6.7}_{-6.2}$
[44–45]	$96.1^{+3.0}_{-6.3}$	$75.0^{+14.1}_{-19.1}$	$66.1^{+4.5}_{-4.7}$	$56.9^{+3.4}_{-3.4}$

Column 1: X-ray luminosity range of the bin in units of  $\text{erg s}^{-1}$  (logarithmic units); columns 2, 3 and 4: fraction of BUXS type 1 and type 2 AGN and SDSS QSO2s in the infrared AGN wedge, respectively; column 5: fraction of SDSS QSO2s in the infrared AGN wedge after applying a median extinction correction to the [O III] line luminosities (see Sec. 3.3 for details).

bottom right of Fig. 4) does not affect our main conclusions.

Fig. 4 (see also Table 3) shows that the fraction of SDSS QSO2s in the infrared AGN wedge is substantially lower than for the BUXS type 1 AGN but it is consistent, within the uncertainties, with that for the BUXS type 2 AGN, especially at the highest luminosities. However, if we correct for extinction all [O III] luminosities using the median Balmer line ratio derived in R08, the fraction of SDSS QSO2s turns out to be significantly lower than that of the BUXS type 2 AGN at  $L_{2-10 \text{ keV}} \lesssim 10^{44} \text{ erg s}^{-1}$  (last column in Table 3). Even if this result must be considered with caution, given the large uncertainties related to the reddening correction, we can conclude that the completeness function of SDSS QSO2s is lower than that of the BUXS type 2 AGN in the low luminosity regime.

The apparent different fractions of BUXS type 1 and type 2 AGN in the infrared AGN wedge, especially at low luminosities, could be explained if all type 2 objects suffer larger extinction at rest-frame optical/near-infrared wavelengths so that, for a given luminosity, their observed WISE fluxes are more contaminated by their host galaxies than

those of type 1 AGN. We note however, that the optical classification of the AGN in BUXS relies on the detection of UV/optical broad emission lines. Therefore, we cannot rule out the possibility that some BUXS type 2 AGN might be indeed low luminosity type 1 AGN where the broad emission lines are diluted by the host galaxy starlight. This may have some effect on the derived fractions of type 1 AGN in the infrared AGN wedge at  $L_{2-10 \text{ keV}} < 10^{44} \text{ erg s}^{-1}$ . However, such effect should be negligible at luminosities  $L_{2-10 \text{ keV}} > 10^{44} \text{ erg s}^{-1}$  (e.g. Caccianiga et al. 2007).

We would expect different fractions of objects in the infrared AGN wedge if the BUXS and SDSS QSO2 surveys target AGN with different host galaxy properties, in the sense that the infrared emission in the BUXS type 2 AGN is less contaminated by the host galaxy than in the SDSS QSO2s at the same luminosity. We will come back to this point in Sec. 5.1. The results presented in this section indicate however, that at high luminosities the infrared AGN wedge seems to be able to unbiasedly select both hard X-ray type 2 AGN and SDSS QSO2s.

### 3.4 Can MIR AGN selection techniques identify luminous heavily obscured AGN?

The results in Sec. 3.3 suggest that at luminosities  $L_{2-10 \text{ keV}} > 10^{44} \text{ erg s}^{-1}$ , the infrared AGN wedge is highly effective at selecting obscured AGN. However, the sample of BUXS AGN does not include any Compton-thick objects. To investigate this we have evaluated whether the SDSS QSO2s identified as Compton-thick candidates in the literature from the studies of Vignali et al. (2010) and Jia et al. (2012) would be selected by the infrared AGN wedge. The Compton-thick classification for these objects is based on their low X-ray/[O III] flux ratios (observed 2-10 keV rest-frame luminosities  $\lesssim 1\%$  of the predicted values based on the [O III]  $\lambda 5007$  line luminosity).

The X-ray follow-up of the SDSS QSO2s in R08 focused mainly on the most luminous objects. Hence, to

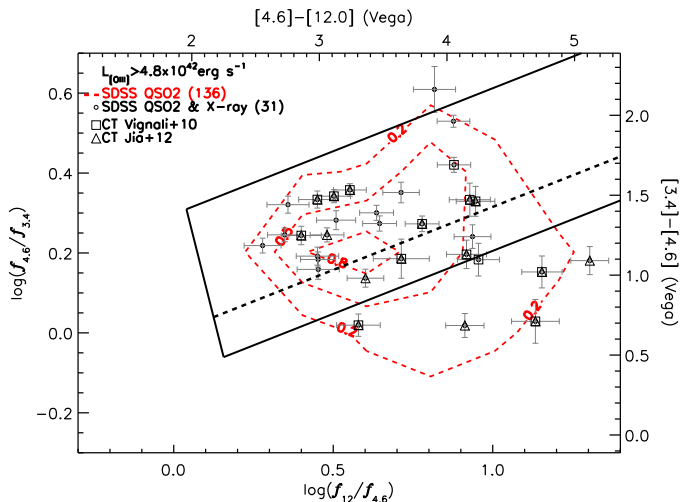


**Figure 5.** MIR colours for the SDSS QSO2s with WISE detections with  $\text{SNR} \geq 5$  at all 3.4, 4.6, and  $12 \mu\text{m}$ ,  $L_{[\text{O III}]} \geq 4.8 \times 10^{42} \text{ erg s}^{-1}$  and X-ray follow-up with either *Chandra* or *XMM-Newton* (open circles). The error bars include both the WISE catalogued flux errors and systematic uncertainties as described in Sec. 2.3. Compton-thick candidates identified in the literature from the studies of Vignali et al. (2010) and Jia et al. (2012) are indicated with open squares and triangles, respectively. Our AGN selection wedge and power-law locus are the thick solid and dashed black lines, respectively. The dashed contours indicate the density (normalized to the peak value) of all SDSS QSO2s with  $L_{[\text{O III}]} \geq 4.8 \times 10^{42} \text{ erg s}^{-1}$ .

include as many objects as possible with available X-ray information, we selected all SDSS QSO2s with WISE detections with  $\text{SNR} \geq 5$  at all 3.4, 4.6, and  $12 \mu\text{m}$  and  $L_{[\text{O III}]} \geq 4.8 \times 10^{42} \text{ erg s}^{-1}$  (136 objects in total). The fraction of those objects in the infrared AGN wedge is  $72.8_{-6.5}^{+5.9}\%$  (99 objects). In total 31 out of 136 objects have observations in the *XMM-Newton* and *Chandra* archives and 24 ( $77.4_{-13.4}^{+10.4}\%$ ) fall in the infrared AGN wedge. This fraction is entirely consistent with that derived for all the objects at the same luminosity showing that by selecting the SDSS QSO2s with X-ray follow-up we are not introducing any bias in terms of infrared colours.

Out of the 31 SDSS QSO2s with X-ray follow-up, 18 objects are identified as Compton-thick candidates. Of these 12 are in the infrared AGN wedge ( $66.7_{-18.5}^{+15.5}\%$ ). Although the number of objects in the comparison is small, the fraction of Compton-thick QSO2 candidates in the infrared AGN wedge is consistent, within the uncertainties, with the value for the full SDSS QSO2 sample at the same luminosities (both with and without X-ray observations). This suggests that at least at the AGN luminosities involved in the comparison, Compton-thick and Compton-thin SDSS QSO2s have similar WISE colour distributions. To illustrate this result, we show in Fig. 5 the WISE colours of the SDSS QSO2s with X-ray follow-up and indicate those objects identified as Compton-thick candidates either from the studies of Vignali et al. (2010) or Jia et al. (2012). The contours in Fig. 5 represent the distribution of colours for all the SDSS QSO2s with  $L_{[\text{O III}]} \geq 4.8 \times 10^{42} \text{ erg s}^{-1}$ . As already indicated, the Compton-thick candidates have a distribution of colours that is consistent with that for the SDSS QSO2s with same luminosities.

These results fully support that at high AGN luminosities and  $z \lesssim 1$  our MIR selection technique is very effective at identifying both Compton-thin and Compton-thick AGN.

## 4 PROPERTIES OF X-RAY AND OPTICALLY SELECTED QSO2

### 4.1 Infrared colours

As shown in Fig. 3, the WISE objects in the BUXS area detected in hard X-rays and the SDSS QSO2s preferentially occupy different regions of the infrared colour-colour diagram. SDSS QSO2s have overall bluer  $\log(f_{4.6}/f_{3.4})$  colours and redder  $\log(f_{12}/f_{4.6})$  colours than the X-ray detected WISE objects. To study this effect in more detail in what follows we restrict our analysis to the objects in the infrared AGN wedge. In these objects the MIR fluxes measured with WISE should be dominated by the AGN.

Fig. 6 (top) shows the distributions of the  $\log(f_{4.6}/f_{3.4})$  and  $\log(f_{12}/f_{4.6})$  colours for the SDSS QSO2s and for all the WISE sources in the BUXS survey area in the infrared AGN wedge with and without detection in X-rays, respectively. In the infrared AGN wedge X-rays preferentially trace the objects with the bluest  $\log(f_{4.6}/f_{3.4})$  and  $\log(f_{12}/f_{4.6})$  colours. Some caution must be taken however, when using  $\log(f_{4.6}/f_{3.4})$  colours as even for objects in the infrared AGN wedge, starlight could contaminate the WISE measured fluxes at the shortest wavelengths. Thus in the following we restrict the comparison to  $\log(f_{12}/f_{4.6})$  colours that should provide a “cleaner” view of the AGN component.

A Kolmogorov-Smirnov (K-S) test indicates that the  $\log(f_{12}/f_{4.6})$  colour distributions of the WISE X-ray non-detected and the SDSS QSO2s are consistent with each other at a  $>99\%$  confidence level (null hypothesis probability 73%). The SDSS QSO2s in R08 trace better than X-ray selection the X-ray-undetected infrared AGN candidates with the reddest colours in the infrared AGN wedge.

Fig. 6 (bottom) shows the  $\log(f_{12}/f_{4.6})$  (and  $\log(f_{4.6}/f_{3.4})$  for comparison) colour distributions for the SDSS QSO2s and for the BUXS type 1 and type 2 AGN, respectively. The BUXS type 2 AGN have overall redder  $\log(f_{12}/f_{4.6})$  colours than the BUXS type 1 AGN, although the dispersion of the distributions is large ( $\sigma \sim 0.12$ ). The mean colour  $\langle \log(f_{12}/f_{4.6}) \rangle$  is 0.37 and 0.43 for the type 1 and type 2 AGN, respectively. A K-S test between the type 1 and type 2 AGN colour distributions shows that they are different at a  $>99\%$  confidence level (null hypothesis probability 0.13%). We obtain the same result when comparing the  $\log(f_{12}/f_{4.6})$  colour distributions of the BUXS type 2 AGN and the SDSS QSO2s. The SDSS QSO2s trace the objects with the reddest  $\log(f_{12}/f_{4.6})$  colours (and also reddest  $\log(f_{4.6}/f_{3.4})$  colours) in the infrared AGN wedge, with  $\langle \log(f_{12}/f_{4.6}) \rangle = 0.62$  and  $\sigma \sim 0.19$ .

#### 4.1.1 Redshift and luminosity effects

In order to compare the observed infrared colours of objects it is important that they span the same range of  $z$  and luminosities. This way we minimize k-correction effects and we account for the luminosity dependence of host galaxy contamination to the observed MIR fluxes

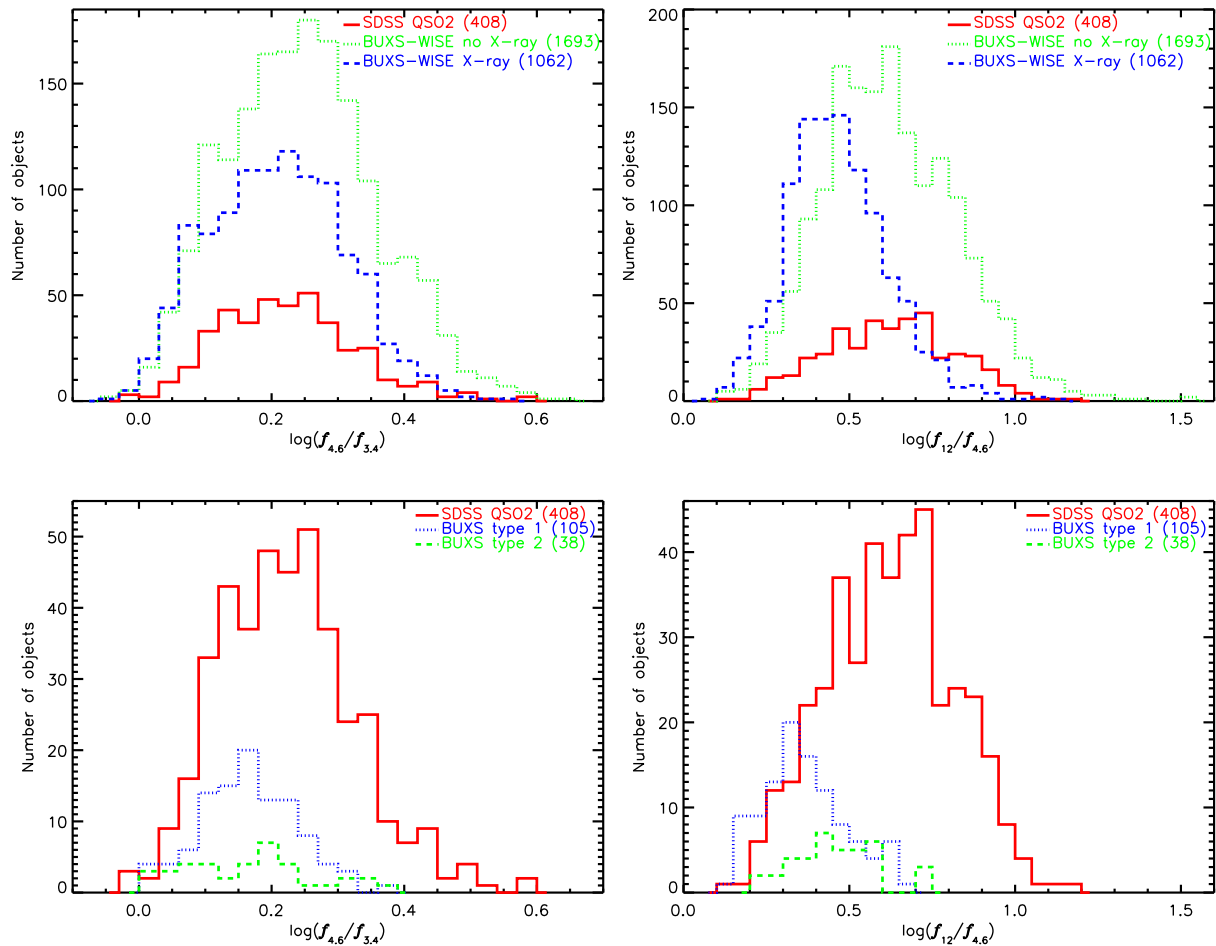


**Figure 6.** Distributions of WISE colours for different classes of objects in the infrared AGN wedge. Top:  $\log(f_{4.6}/f_{3.4})$  (left) and  $\log(f_{12}/f_{4.6})$  (right) colour distributions for the SDSS QSO2s (solid line histograms) and for all the WISE objects in the BUXS area (i.e. not applying any of the X-ray selection criteria that define the BUXS AGN sample, see Sec. 2.3.2 and Table 1) with and without detection in X-rays, respectively (dashed and dotted line histograms). Bottom:  $\log(f_{4.6}/f_{3.4})$  (left) and  $\log(f_{12}/f_{4.6})$  (right) colour distributions for the SDSS QSO2s (solid line histograms) and for the type 1 and type 2 AGN in the BUXS survey (dotted and dashed line histograms).

(e.g. Cardamone et al. 2008; Assef et al. 2012; Donley et al. 2012; M12; Stern et al. 2012). Fig. 7 shows the  $z$  (top) and 2-10 keV luminosity (middle) distributions of the BUXS AGN and the SDSS QSO2s. The BUXS type 2 AGN and SDSS QSO2s span the same  $z$  range, therefore it does not appear that k-correction effects alone can explain their different MIR colour distributions.

On the other hand, according to the predicted 2-10 keV luminosities<sup>3</sup> the SDSS QSO2s are intrinsically more luminous than the BUXS type 2 AGN. A K-S test gives a probability higher than 99.99% that the two distributions are different. This difference should be somewhat larger if we consider that the [O III]  $\lambda 5007$  luminosities were not corrected for extinction (see Sec. 3.3). To confirm this result in Fig. 7 (bottom) we show the distributions of rest-frame  $6 \mu\text{m}$

monochromatic luminosities. At these wavelengths the emission should suffer little contamination from star formation processes in the host galaxy (e.g. Nardini et al. 2009, 2010) and should be much less affected by dust extinction than the optical [O III] line. Therefore, rest-frame luminosities at  $6 \mu\text{m}$  are a robust independent proxy of the AGN intrinsic power. The  $6 \mu\text{m}$  luminosities were computed from linear interpolation of the WISE observed fluxes (see Sec. 4.2 for more details). A K-S test gives a 99.5% probability that the  $6 \mu\text{m}$  luminosity distributions for the BUXS type 2 AGN and the SDSS QSO2s are different.

Both monochromatic  $6 \mu\text{m}$  (rest-frame) continuum and 2-10 keV predicted luminosities indicate that the SDSS QSO2s are on average  $\sim 20\text{-}30\%$  more luminous than the BUXS type 2 AGN. Although the overlap in the luminosity distributions is large, it is reasonable to expect that at the shortest WISE wavelengths starlight contamination from the blue infrared hosts might be more important in the intrinsically less luminous BUXS type 2 AGN.

The type 1 AGN in BUXS have the highest luminosities in this comparison and the bluest infrared colours. Be-

<sup>3</sup> We have not used in the comparison [O III] luminosities for the BUXS AGN as not all the spectra sample the rest-frame wavelengths of the [O III] line and in many cases the SNR is not sufficient to obtain accurate measurements of the line luminosity.

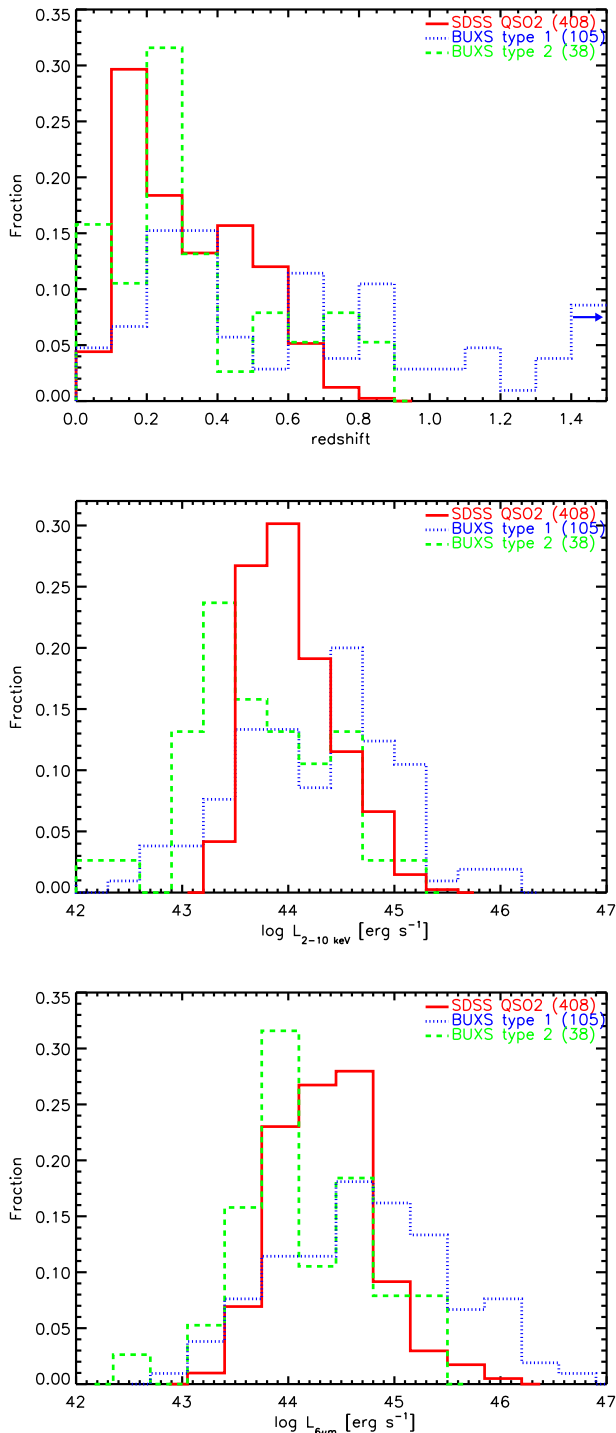


**Figure 7.** Comparison of the  $z$  (top), 2-10 keV (middle) and  $6\ \mu\text{m}$  luminosity (in logarithmic units) distributions for the SDSS QSO2s in R08 and the BUXS type 1 and type 2 AGN, respectively. For the SDSS QSO2s the 2-10 keV luminosities were derived from the empirical relation between X-ray and [O III]  $\lambda 5007$  luminosities of J12 (see Sec. 3.3). For the BUXS AGN the X-ray luminosities were derived from the modeling of their X-ray spectra and are corrected for intrinsic absorption. The monochromatic  $6\ \mu\text{m}$  (rest-frame) luminosities were derived using linear interpolation between WISE nearby bands.

cause the type 1 AGN span a broad range of  $z$ , their blue MIR colours could be the result of sampling shorter rest-frame wavelengths. To evaluate this effect we have compared the  $\log(f_{12}/f_{4.6})$  colour distributions for the type 1 AGN at  $z \leq 0.6$  and  $z > 0.6$  (similar number of objects on each bin). A K-S test indicates that the two colour distributions are consistent (null hypothesis probability 13.5%). Higher  $z$  (more luminous) type 1 AGN tend to have redder infrared colours. Thus, k-correction effects cannot explain the different colour distributions of the BUXS type 1 AGN and the X-ray and optically selected type 2 AGN in the infrared AGN wedge.

## 4.2 Median spectral energy distributions

To understand the nature and properties of the AGN selected using WISE colours, we have computed the median UV-to-MIR rest-frame SEDs of the BUXS AGN and SDSS QSO2s in the infrared AGN wedge. Ideally this should be performed on the individual SEDs, to avoid the uncertainties associated with the important dispersion in SED properties even amongst objects in the same AGN class (e.g. Krawczyk et al. 2013; Elvis et al. 1994, 2012; Lusso et al. 2011; Richards et al. 2006). Unfortunately, with the existing data we do not have sufficient spectral coverage, especially at infrared wavelengths (only four WISE points from 3 to  $22\ \mu\text{m}$ ), to properly characterize the individual SEDs.

For each object we make use of the WISE all-sky data release in combination with optical photometry from SDSS in the  $u$ ,  $g$ ,  $r$ ,  $i$  and  $z$  bands (Fukugita et al. 1996) and observations in the  $Y$ ,  $J$ ,  $H$  and  $K$  near-infrared bands from the UKIDSS Large Area Survey (LAS) ninth data release (Lawrence et al. 2007). For details on the UKIDSS photometric system, calibration and pipeline processing please refer to Hewett et al. (2006), Hodgkin et al. (2009) and Hambly et al. (2008), respectively. A conservative 5% error was added in quadrature to the SDSS and UKIDSS catalogued flux errors to account for the uncertainties in the zero-points (for WISE fluxes see Sec. 2.3). To obtain the near-infrared counterparts of the SDSS QSO2s we cross-matched the optical positions with the UKIDSS LAS using a 2 arcsec search radius. UKIDSS data is available for  $\sim 41\%$  of the SDSS QSO2s. We note that  $\sim 54\%$  of the SDSS QSO2s have detections in at least one of the Two-Micron All-Sky Survey (2MASS; Skrutskie et al. 2006) filters, most of these objects being at  $z < 0.3$ . However, to avoid biasing the median SEDs at rest-frame near-infrared wavelengths towards the objects with the brightest host galaxies (i.e. near-infrared bright SED shapes), we only used the data from UKIDSS that it is three magnitudes deeper than 2MASS.

To compute the median SEDs we shifted the individual SEDs to a common rest-frame wavelength grid. Because the aim of this analysis is to investigate the overall shape of the observed SEDs, we do not apply any corrections for host galaxy contamination. However the fluxes are corrected for Galactic reddening. We converted the fluxes to luminosities in  $\nu L_\nu$  units and finally, we normalised the SEDs at  $6\ \mu\text{m}$  rest-frame. At this wavelength we should get a relatively uncontaminated view of the AGN while the effects of extinction should be small (e.g. Lutz et al. 2004). The  $6\ \mu\text{m}$  luminosities were computed with linear interpolation between nearby points in  $\log \nu L_\nu$  versus  $\log \lambda$  space. The data were combined and grouped in wavelength bins containing at

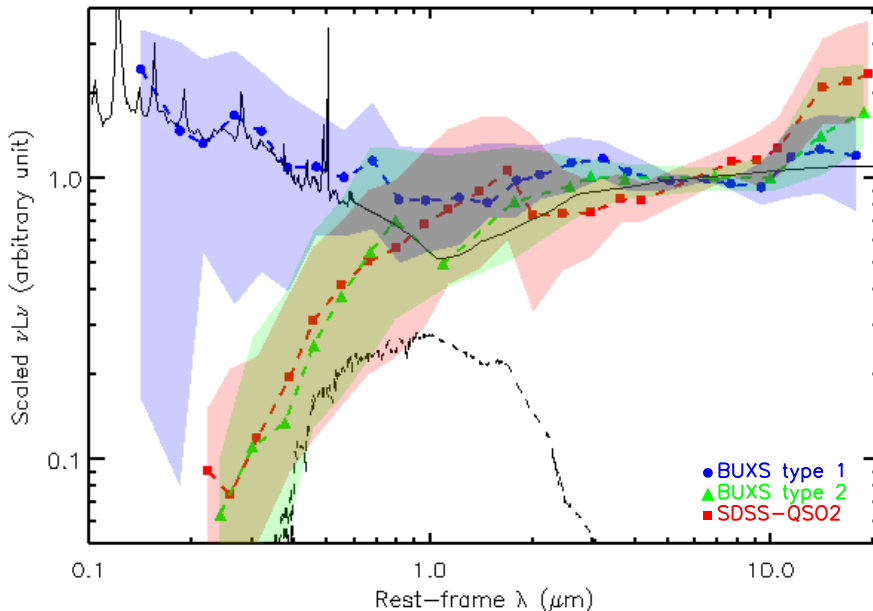


**Figure 8.** Median UV-to-MIR SEDs of the different classes of AGN in the infrared AGN wedge. The SEDs are normalised at  $6\ \mu\text{m}$  rest-frame. Squares for the SDSS QSO2s, circles for the BUXS type 1 AGN and triangles for the BUXS type 2 AGN, respectively. The points are connected with a power-law in linear space (dashed lines). The shaded regions in the figure represent the dispersion in the data points quantified with the 68.27% percentiles. For comparison we show two templates from the library of Polletta et al. (2007): a type 1 QSO normalised at  $6\ \mu\text{m}$  rest-frame (solid line) and an elliptical galaxy with an arbitrary normalization (dashed line).

least 15 points. We required a minimum bin size of  $0.08\ \mu\text{m}$  in logarithmic wavelength. Linear interpolation was used to convert the photometry to the grid points. The luminosity on each bin is the median of the data points, while the dispersion is represented with the percentiles for a 68.27% confidence.

Fig. 8 shows the median SEDs in  $\nu L_\nu$  versus  $\lambda$ . For comparison we show a type 1 AGN template SED and an elliptical galaxy from the Spitzer Wide-area InfraRed Extragalactic survey (SWIRE) library of Polletta et al. (2007). At rest-frame UV/optical wavelengths the BUXS type 1 AGN have the characteristic blue bump continuum typical of the primary emission from the central accretion disk with a change in slope at around  $\sim 1\text{--}2\ \mu\text{m}$  rest-frame. At these wavelengths, however, the median SED is rather flat not showing a clear  $\sim 1\ \mu\text{m}$  inflection point between the UV and near-infrared bumps (Elvis et al. 1994, 2012; Richards et al. 2006). This is most likely due to significant contamination from the hosts. This is not surprising as host galaxy corrections can be important even for luminous type 1 AGN (e.g. Elvis et al. 1994). For the BUXS type 2 AGN and SDSS QSO2s their red UV/optical continuum emission is most likely due to starlight and/or a reddened AGN. This is expected as the classification as a type 2 AGN is based on the lack of sight of the nuclear emission and broad-line region. Fig. 8 shows that the near-infrared stellar bump at  $1.6\ \mu\text{m}$  is clearly more prominent in the SDSS QSO2s. As the median SEDs are normalised at  $6\ \mu\text{m}$  rest-frame luminosities where the emission should be dominated by the AGN, this suggests that the SDSS QSO2s in R08 reside in more luminous hosts.

At wavelengths  $\gtrsim 2\ \mu\text{m}$  (rest-frame) the median SED of the type 1 AGN shows an apparent infrared-bump centered at around  $3\ \mu\text{m}$ . This feature has been interpreted as the signature of the hottest dust component originating in the

inner parts of the obscuring torus (see e.g. Neugebauer et al. 1979; Glikman, Helfand, & White 2006; Netzer et al. 2007). At these wavelengths the median SED of the BUXS type 2 AGN is marginally redder than that of the BUXS type 1 AGN, and the SDSS QSO2s have the reddest continuum. These results are entirely consistent with the observed differences in the distributions of their infrared colours (see Sec. 4.1 and Fig. 6).

Above  $\sim 10\ \mu\text{m}$  all the SEDs show an apparent excess of MIR emission when compared with the type 1 AGN template. This excess is more significant for the SDSS QSO2s. Although the WISE survey at  $22\ \mu\text{m}$  is significantly shallower than those at 3.4, 4.6, and  $12\ \mu\text{m}$ , most SDSS QSO2s and BUXS AGN have  $22\ \mu\text{m}$  detections with at least  $\text{SNR} \geq 2^4$ . For the SDSS QSO2s, 93.4% have  $22\ \mu\text{m}$  detections with  $\text{SNR} \geq 5$  and all but one have  $22\ \mu\text{m}$  detections with  $\text{SNR} \geq 2$ . Thus, it is unlikely that the median SEDs are biased towards the brightest objects at  $22\ \mu\text{m}$ .

#### 4.2.1 SED fitting with templates

To provide a clearer description of the median SEDs we fitted the data with a combination of the type 1 AGN (QSO1) template and one of the galaxy templates from the library of Polletta et al. (2007). The galaxy templates we used comprise elliptical, spiral as well as the starburst templates for I22491, M82, N6090 and Arp220. We selected the fit with the lowest reduced  $\chi^2$ . To account for obscuration of the nuclear AGN light we applied the Small Magellanic Cloud (SMC)-like dust-reddening laws from Gordon et al. (2003) below  $8100\ \text{\AA}$  and Cardelli, Clayton, & Mathis (1989) at longer

<sup>4</sup> Below  $\text{SNR}=2$  WISE flux measurements are considered upper limits (Cutri et al. 2012).

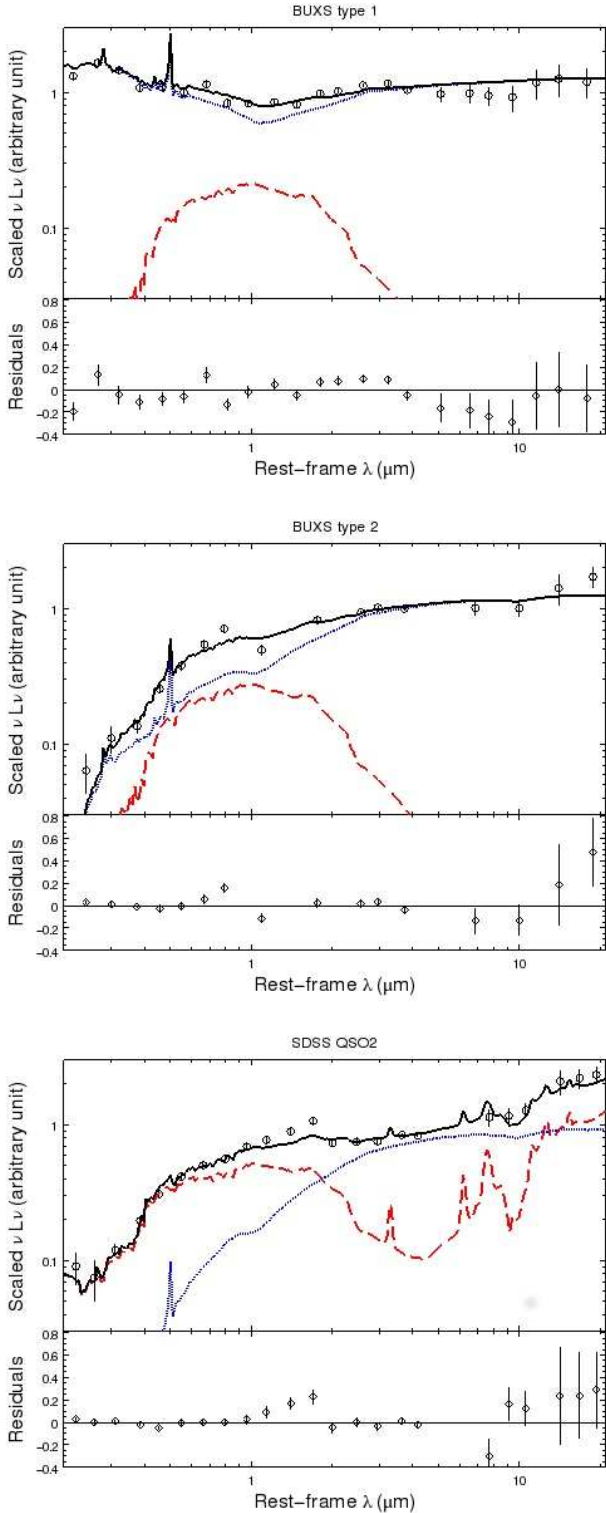


**Figure 9.** Median SEDs of the BUXS type 1 (top) and type 2 (middle) AGN and the SDSS QSO2s (bottom) that fall in the infrared AGN wedge. The data points are indicated with open circles. The error bars are the mean of the flux errors for the individual data points in the bin. The best-fit models are illustrated with the solid lines while the AGN and host galaxy components are illustrated with the dotted and dashed lines, respectively.

wavelengths. With this approach we allow two distinct components, a dusty central structure (warm AGN-heated dust) and an extended star-forming region (cold starburst-heated dust), to contribute to the infrared emission, and a screen-like dusty absorber that reddens the AGN nuclear emission.

In a more physically motivated characterisation of the SEDs the UV/optical emission from the accretion disk and the infrared emission from the torus should be modelled independently. A screen-like nuclear extinction should only be applied to the accretion disk emission while the torus parameters (e.g. viewing angle, optical depth, number of clouds, opening angle, torus size) are incorporated in the different AGN torus model realizations. Unfortunately, these models, especially those where the absorber is clumpy which are strongly supported by observations, have a very large number of parameters (e.g. Nenkova, Ivezić, & Elitzur 2002; Hönig et al. 2006; Nenkova et al. 2008a, 2008b; Schartmann et al. 2008; Heymann & Siebenmorgen 2012). Our median SEDs do not have sufficient spectral resolution to obtain any meaningful constraints on the parameters of the dusty torus. However, as we will see in Sec. 4.2.2 and Sec. 4.2.3, the best-fit extinctions are small and therefore it is reasonable to assume that the screen-like absorber in our models only has an effect on the accretion disk emission component. As the goal of this analysis is to obtain a rough description of the median SEDs by disentangling the AGN and host galaxy emission, the best-fit parameters should only be used as a guide of the overall behaviour in the different classes of objects. The results of the SED fitting are shown in Fig. 9.

#### 4.2.2 SEDs of X-ray selected type 1 and type 2 AGN

The QSO1 template from Polletta et al. (2007) provides a fair representation of the median UV to MIR SED of the BUXS type 1 AGN (best-fit  $\chi^2_\nu=3.4$ ). At rest-frame optical/near-infrared wavelengths there is contamination from starlight. This component is best modelled with an elliptical galaxy template. At MIR wavelengths the emission is clearly dominated by the AGN although the residuals of the fit suggest that the continuum is somewhat bluer than in the QSO1 template.

For the BUXS type 2 AGN both stellar emission (also best modelled with an elliptical galaxy template) and a reddened AGN continuum (best-fit  $N_H = 7.9 \pm 0.4 \times 10^{21} \text{ cm}^{-2}$  or  $A_V \sim 0.6$  assuming the SMC dust-to-gas ratio; Gordon et al. 2003) are required to provide a good quality fit ( $\chi^2_\nu=2.4$ ) at rest-frame UV/optical wavelengths. The MIR emission is dominated by the AGN and there is no evidence of star-forming activity. This is an expected result as the median SEDs were derived using only the objects in the infrared AGN wedge.

As a test we also fitted the BUXS type 2 AGN median SED with the QSO2 SED template from Polletta et al. (2007) as it should provide a more accurate representation of the typical MIR continuum for luminous type 2 AGN. This template also provides a good quality fit at MIR wavelengths and confirms that the MIR continuum of the BUXS type 2 AGN in the infrared AGN wedge is dominated by the AGN component.

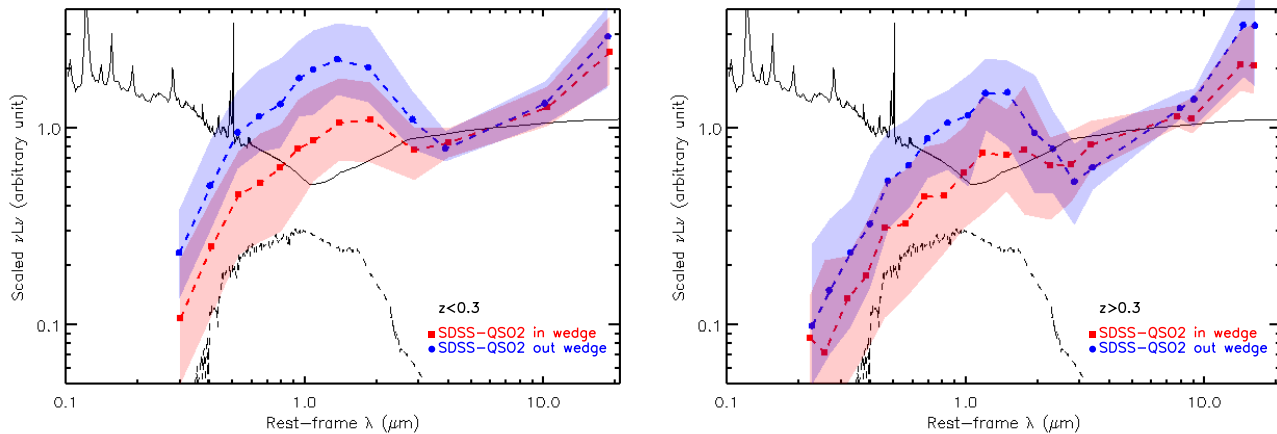


**Figure 10.** Median UV-to-MIR SEDs for the SDSS QSO2s in and out the infrared AGN wedge, respectively. The SEDs are normalised at  $6\ \mu\text{m}$  rest-frame. Left: SDSS QSO2s at  $z \leq 0.3$ . Right: SDSS QSO2s at  $z > 0.3$ . The points are connected with a power-law in linear space (dashed lines). The shaded regions in the figure represent the dispersion in the data points quantified with the 68.27% percentiles. For comparison we show two templates from the library of Polletta et al. (2007): a type 1 QSO normalised at  $6\ \mu\text{m}$  rest-frame (solid line) and an elliptical galaxy with an arbitrary normalization (dashed line).

#### 4.2.3 SEDs of SDSS QSO2s

At the wavelengths sampled by our data the contribution from the host galaxy to the median SED of the SDSS QSO2s is more important than in the BUXS type 2 AGN. An acceptable fit could only be obtained with a composite SED where a reddened AGN continuum (best-fit  $N_{\text{H}} = 1.3 \pm 0.2 \times 10^{22}\ \text{cm}^{-2}$  or  $A_{\text{V}} \sim 1$  assuming the SMC dust-to-gas ratio; Gordon et al. 2003), stellar emission and features associated with star formation activity contribute to the observed fluxes. The best-fit was obtained with the star-forming galaxy SED of M82 ( $\chi^2_{\nu} = 2.2$ ; see Fig. 9, bottom). Still the MIR emission in these objects is dominated by the AGN. This is expected as the median SED was derived for the SDSS QSO2s in the infrared AGN wedge.

At optical/near-infrared wavelengths both the AGN and stellar emission are required to provide a good quality fit although the AGN contribution is not as important as in the BUXS type 2 AGN. None of the star-forming templates in the library of Polletta et al. (2007) can fit the near-infrared stellar bump. The most plausible explanation for this result is that we are combining the SEDs of a large number of objects with a range in host galaxy properties. We also checked that the QSO2 template from Polletta et al. (2007) also provides a good quality fit to the data points at MIR wavelengths, reaching similar conclusions.

In Sec. 4.1, from the comparison of the  $\log(f_{12}/f_{4.6})$  colour distributions of the BUXS type 1 and type 2 AGN and the SDSS QSO2s, we found a trend where higher (line of sight) absorption might be associated with redder infrared colours. However we have shown that, even for luminous AGN in the infrared AGN wedge, host galaxy contamination of the WISE fluxes can have an effect on the observed properties of the objects. Our results suggest that it is not the possible presence of Compton-thick AGN that determines the red MIR continuum of the SDSS QSO2s but most likely the properties of their host galaxies.

## 5 DISCUSSION

The results of the analysis of the median SEDs of the SDSS QSO2s are entirely consistent with those obtained from *Spitzer* MIR spectroscopy of QSO2s selected from optical SDSS observations (e.g. Zakamska et al. 2008). The MIR spectra of these objects show a large diversity of properties. While some objects show a featureless continuum, star formation activity is detected in most QSO2s although the MIR emission is dominated by the AGN. In the study of a sample of SDSS galaxies at  $z < 0.3$  Kauffmann et al. (2003) suggested a connection between the AGN power and star formation activity. A young stellar population and signatures of recent bursts of star formation are a general property for the most powerful QSO2s. A similar result was found by Vanden Berk et al. (2006) for SDSS selected type 1 AGN at  $z < 0.75$ . This is consistent with our finding that star formation is a general property in the most luminous (the sources that preferentially enter the infrared AGN wedge) SDSS QSO2s.

### 5.1 Understanding the MIR continuum emission of SDSS QSO2s

As noted in Sec. 4.2 (see also Fig. 8 and Fig. 9) the SDSS QSO2s have more pronounced near-infrared stellar bumps. We explain this as a selection effect due to the tight magnitude limits applied by the SDSS spectroscopic target selection algorithms. For example, the Galaxy algorithm selects resolved objects with Petrosian magnitudes  $r < 17.77$  mag while the Low- $z$  and High- $z$  QSO algorithms target objects with point spread function (PSF) magnitudes  $15 < i < 19.1$  and  $15 < i < 20.2$ , respectively. The Serendipity FIRST algorithm selects sources with fiber magnitudes  $14 < g, r, i < 20.5$ . For comparison, the BUXS AGN span a much broader range of optical magnitudes,  $15 < r < 23.5$ , where  $r$  refers to SDSS PSF magnitudes. Because the host galaxy stellar emission is an important component at UV/optical wavelengths in type 2 AGN, the magnitude limits of the SDSS spectroscopy are likely biasing the samples towards type 2 objects with more luminous (more massive) hosts. This can reduce the com-

pleteness of the infrared AGN wedge for selection of SDSS QSO2s as such techniques preferentially miss AGN in massive hosts. This is actually what we find when comparing the effectiveness of the infrared AGN wedge for the BUXS type 2 AGN and the SDSS QSO2s (see Sec. 3.3): the selection completeness for the SDSS QSO2s is lower than that of the BUXS type 2 AGN, at least in the low luminosity regime.

To illustrate the host galaxy dilution effect we show in Fig. 10 the median SEDs for the SDSS QSO2s at  $z \leq 0.3$  (left) and  $z > 0.3$  (right) that are in/out the infrared AGN wedge (normalized at  $6 \mu\text{m}$  rest-frame), respectively. The objects outside the infrared AGN wedge reside in more massive hosts. The host galaxy emission contaminates the WISE fluxes at the shortest wavelengths, an effect that becomes more important at higher  $z$  due to the k-correction. Based on the existing data we do not find significant differences in the MIR continuum of the SDSS QSO2s in and out the infrared AGN wedge. Although we cannot quantify the role of dust extinction in shaping the MIR spectra, we would expect that star formation features would be stronger in the objects with more massive galaxies. Obscured AGN normally reside in optically luminous massive galaxies (stellar masses  $M_* \gtrsim 10^{10-11} M_\odot$ ; Babić et al. 2007; Alonso-Herrero et al. 2008; Brusa et al. 2009; Mainieri et al. 2011). If the SDSS QSO2s follow the correlation between the specific star formation rate, i.e the star formation rate per unit stellar mass, and  $M_*$  in local star-forming galaxies (e.g. Brinchmann et al. 2004; Salim et al. 2005) it is reasonable to expect the detection of star formation signatures in these objects.

We note that obscuration by gas in the host galaxy on scales of hundreds of parsecs (e.g. starbursts, edge-on discs) might also be responsible for the UV/optical reddening measured in the median SEDs of the BUXS type 2 AGN and the SDSS QSO2s. Observational evidence for this effect is supported by studies of the host galaxy properties of optically selected AGN (Maiolino & Rieke 1995; Lagos et al. 2011). For example, the study of Lagos et al. (2011), based on the SDSS spectroscopic survey, finds a tendency for type 1 AGN to reside on face-on systems while type 2 objects, especially those with high [O III] equivalent widths, reside preferentially on edge-on systems. Thus, host galaxy obscuration might have a more important role in the SDSS QSO2s than in the BUXS type 2 AGN.

Finally, we stress that it is unlikely that QSO2 samples based on the [O III] line emission, such as the R08 catalogue, are biased towards objects with more intense star formation activity. As shown in Kauffmann et al. (2003), [O III]  $\lambda 5007$  emission is relatively weak in metal-rich star-forming galaxies, with star formation contributing only a few percent to the [O III] fluxes. A more recent work by LaMassa et al. (2010) finds no strong evidence that [O III] selection is biased towards AGN with strong star formation activity.

## 5.2 Identifying AGN with X-ray, optical and MIR surveys

Hard X-ray surveys ( $> a$  few keV) provide the most complete and reliable census of AGN since they suffer little contamination from processes not related to SMBH activity, missing only Compton-thick sources. As hard X-ray emission is not affected by host galaxy dilution, these surveys can identify

the AGN residing in the most massive galaxies and/or with more intense star formation and can identify a large population of low luminosity AGN.

On the other hand, [O III]  $\lambda 5007$  selection is less sensitive to circumnuclear obscuration. Therefore, it is an efficient and powerful technique to provide a more complete view of the heavily obscured and Compton-thick AGN population. However, such selection depends on empirical emission-line ratio diagnostic diagrams which are known to misidentify many faint AGN in star-forming galaxies (Trouille & Barger 2010). Indeed, a significant fraction of X-ray selected AGN, mainly at  $L_{2-10 \text{ keV}} < 10^{43}$ , have optical spectra dominated by the host galaxy and without signatures of AGN activity (e.g. Caccianiga et al. 2007). Thus, [O III]-based surveys suffer from effects associated with host galaxy dilution. They will be incomplete at low luminosities and for objects in which the narrow line region is heavily extinguished.

MIR based surveys are a promising technique to identify absorbed AGN missed in X-ray surveys, as most of the absorbed radiation should be re-emitted by dust at these wavelengths. The results presented in this paper support that WISE colour-based MIR selection techniques are able to identify luminous heavily absorbed and even Compton-thick AGN at least up to  $z \lesssim 1$ . The best candidates are those objects in the infrared AGN wedge with the reddest MIR colours. However, it is important to note that MIR selection identifies predominantly luminous AGN. At low luminosities, especially for those objects with large extinction at rest-frame infrared wavelengths, the selection is largely incomplete and strongly biased against AGN residing in massive and/or star-forming hosts. This will be more important at higher  $z$  due to the k-correction. This observational bias needs to be taken into account for example when studying the coevolution of SMBH and their host galaxies.

## 6 CONCLUSIONS

The main goal of this work was to evaluate whether AGN selection techniques in the infrared with WISE, such as the infrared AGN wedge presented in M12, are able to identify with high efficiency absorbed AGN missed in X-rays. We also studied the properties of the AGN populations independently selected in X-ray and optical surveys. To this aim we used the largest catalogue of optically selected QSO2s at  $z \leq 0.83$  in SDSS. These objects were selected on the basis of their high [O III]  $\lambda 5007$  line luminosities,  $L_{[\text{O III}] \lambda 5007} \geq 10^{8.3} L_\odot$ . Such a selection should be relatively unbiased against heavy obscuration. We then compared the results with those for the hard ( $> 4.5$  keV) X-ray selected AGN in the BUXS survey.

The fraction of SDSS QSO2s in the infrared AGN wedge is a strong function of the AGN luminosity. In total,  $53.3 \pm 3\%$  of all the SDSS QSO2s with detection in all the three shortest wavelength bands of WISE fall in the infrared AGN wedge. This fraction increases to  $66.1^{+4.5}_{-4.7}\%$  at the highest [O III] luminosities, from  $\sim 2.2 \times 10^{42}$  to  $2.5 \times 10^{43} \text{ ergs}^{-1}$ . This is substantially lower than for the BUXS type 1 AGN in the same luminosity range, but it is consistent within the uncertainties, with that obtained for the BUXS type 2 AGN.

To evaluate whether our infrared selection technique

identifies Compton-thick AGN, we compiled a sample of SDSS QSO2s identified as Compton-thick candidates in the literature. We found that the fraction of SDSS QSO2s that are Compton-thick candidates and fall in the infrared AGN wedge is consistent, within the uncertainties, with the fraction of objects in the full sample that fall in that zone ( $66.7^{+15.5}_{-18.5}\%$  versus  $77.4^{+10.4}_{-13.4}\%$ ). Furthermore, at the AGN luminosities involved in the comparison, Compton-thick and Compton-thin SDSS QSO2s have similar WISE colour distributions.

Considering only the objects in the infrared AGN wedge to minimize host galaxy contamination, we found that the BUXS type 1 AGN have bluer  $\log(f_{12}/f_{4.6})$  colours than the type 2 AGN, and the SDSS QSO2s trace the objects with the reddest colours. The SDSS QSO2s trace better than X-ray selection the X-ray undetected WISE AGN candidates in the BUXS survey area with the reddest colours in the wedge. These results suggest a trend where higher (line of sight) absorption might be associated with redder  $\log(f_{12}/f_{4.6})$  colours.

To understand the nature and properties of the AGN candidates identified with WISE we analysed the median UV-to-MIR rest-frame SEDs of the AGN in BUXS and the SDSS QSO2s in the infrared AGN wedge. Both an extinguished AGN continuum and host galaxy stellar emission, are required to fully account for the rest-frame UV/optical/near-infrared SEDs of the BUXS type 2 AGN and SDSS QSO2s. Even for the SDSS QSO2s the measured extinction is not sufficiently large to fully suppress the nuclear emission at these wavelengths.

The SDSS QSO2s have more pronounced near-infrared stellar bumps than both the type 1 and type 2 AGN in BUXS. The tight magnitude limits applied by the SDSS spectroscopic target algorithms, especially at  $z \leq 0.3$ , are likely biasing type 2 AGN samples towards objects with more luminous (more massive) hosts. It does not appear that either  $z$  or luminosity effects can explain these differences.

The MIR continuum of both the BUXS AGN and SDSS QSO2s is dominated by the AGN component. No clear features of star-forming activity were detected in the MIR median SEDs of the BUXS type 1 and type 2 AGN. However MIR excess emission is a general property of the SDSS QSO2s. We interpret this as features associated with star-forming activity in the AGN host galaxies. The combination of extinction at rest-frame optical/near-infrared wavelengths and contamination from the more massive host galaxies at the longest MIR wavelengths naturally explains the red WISE colours and MIR continua of the SDSS QSO2s. Host galaxy dilution is an important effect at MIR wavelengths that may strongly bias the AGN populations identified with WISE colour-based techniques, especially at low luminosities, against AGN in very massive/star-forming hosts.

We conclude that at high luminosities and  $z \lesssim 1$  our MIR selection technique is very efficient at identifying both Compton-thin and Compton-thick AGN. Although optical/near-infrared spectroscopy is essential to reveal the true nature of infrared-selected AGN, as pointed out in M12, the best WISE candidates to account, at least in part, for the absorbed luminous AGN missed in X-rays are the objects with the reddest MIR colours in the wedge.

## ACKNOWLEDGMENTS

This work is based on observations obtained with *XMM-Newton*, an ESA science mission with instruments and contributions directly funded by ESA Member States and NASA. Based on data from the Wide-field Infrared Survey Explorer, which is a joint project of the University of California, Los Angeles, and the Jet Propulsion Laboratory/California Institute of Technology, funded by the National Aeronautics and Space Administration. Funding for the SDSS and SDSS-II has been provided by the Alfred P. Sloan Foundation, the Participating Institutions, the National Science Foundation, the U.S. Department of Energy, the National Aeronautics and Space Administration, the Japanese Monbukagakusho, the Max Planck Society, and the Higher Education Funding Council for England. The SDSS Web Site is <http://www.sdss.org/>. Based on observations collected at the European Organisation for Astronomical Research in the Southern Hemisphere, Chile, programme IDs 084.A-0828, 086.A-0612, 087.A-0447 and 088.A-0628. Based on observations made with the William Herschel Telescope and its service programme -operated by the Isaac Newton Group-, the Telescopio Nazionale Galileo -operated by the Centro Galileo Galilei and the Gran Telescopio de Canarias installed in the Spanish Observatorio del Roque de los Muchachos of the Instituto de Astrofísica de Canarias, in the island of La Palma. SM and FJC acknowledge financial support by the Spanish Ministry of Economy and Competitiveness through grant AYA2010-21490-C02-01. SM acknowledge financial support from the JAE-Doc program (Consejo Superior de Investigaciones Científicas, cofunded by FSE). A.A.-H. acknowledges support from the Universidad de Cantabria through the Augusto G. Linares program. A.B. acknowledges a Royal Society Wolfson Research Merit Award. P.S. acknowledges financial support from ASI (grant No. I/009/10/0). A.R. acknowledges support from an IUCAA post-doctoral fellowship. The authors thank A. Hernán Caballero for useful suggestions. The authors wish to thank the anonymous referee for constructive comments.

## REFERENCES

- Alexander D. M., et al., 2003, *AJ*, 126, 539
- Alonso-Herrero A., et al., 2006, *ApJ*, 640, 167
- Alonso-Herrero A., Pérez-González P. G., Rieke G. H., Alexander D. M., Rigby J. R., Papovich C., Donley J. L., Rigopoulou D., 2008, *ApJ*, 677, 127
- Assef R. J., et al., 2012, arXiv:1209.6055
- Babić A., Miller L., Jarvis M. J., Turner T. J., Alexander D. M., Croom S. M., 2007, *A&A*, 474, 755
- Ballantyne D. R., Draper A. R., Madsen K. K., Rigby J. R., Treister E., 2011, *ApJ*, 736, 56
- Barvainis R., 1987, *ApJ*, 320, 537
- Bassani L., Dadina M., Maiolino R., Salvati M., Risaliti G., della Ceca R., Matt G., Zamorani G., 1999, *ApJS*, 121, 473
- Brandt W. N., Hasinger G., 2005, *ARA&A*, 43, 827
- Brandt W. N., Alexander D. M., 2010, *PNAS*, 107, 7184
- Brinchmann J., Charlot S., White S. D. M., Tremonti C., Kauffmann G., Heckman T., Brinkmann J., 2004, *MNRAS*, 351, 1151
- Brusa M., et al., 2009, *A&A*, 507, 1277
- Burlon D., Ajello M., Greiner J., Comastri A., Merloni A., Gehrels N., 2011, *ApJ*, 728, 58
- Caccianiga A., et al., 2004, *A&A*, 416, 901
- Caccianiga A., Severgnini P., Della Ceca R., Maccacaro T., Carrera F. J., Page M. J., 2007, *A&A*, 470, 557

- Cardamone C. N., et al., 2008, *ApJ*, 680, 130
- Cardelli J. A., Clayton G. C., Mathis J. S., 1989, *ApJ*, 345, 245
- Comastri A., et al., 2011, *A&A*, 526, L9
- Cutri R. M., et al., 2012, *wise.rept*, 1
- Della Ceca R., et al., 2008, *A&A*, 487, 119
- Donley J. L., Koekemoer A.M., et al. 2012, *ApJ*, 748, 142
- Eckart M. E., McGreer I. D., Stern D., Harrison F. A., Helfand D. J., 2010, *ApJ*, 708, 584
- Elitzur M., 2012, *ApJ*, 747, L33
- Elvis M., et al., 1994, *ApJS*, 95, 1
- Elvis M., et al., 2012, *ApJ*, 759, 6
- Fiore F., et al., 2008, *ApJ*, 672, 94
- Fukugita M., Ichikawa T., Gunn J. E., Doi M., Shimasaku K., Schneider D. P., 1996, *AJ*, 111, 1748
- Georgantopoulos I., Georgakakis A., Rowan-Robinson M., Roviolo E., 2008, *A&A*, 484, 671
- Gilli R., Comastri A., Hasinger G., 2007, *A&A*, 463, 79
- Glikman E., Helfand D. J., White R. L., 2006, *ApJ*, 640, 579
- Goulding A. D., Alexander D. M., Mullaney J. R., Gelbord J. M., Hickox R. C., Ward M., Watson M. G., 2011, *MNRAS*, 411, 1231
- Gordon K. D., Clayton G. C., Misselt K. A., Landolt A. U., Wolff M. J., 2003, *ApJ*, 594, 279
- Hambly N. C., et al., 2008, *MNRAS*, 384, 637
- Heckman T. M., Ptak A., Hornschemeier A., Kauffmann G., 2005, *ApJ*, 634, 161
- Hewett P. C., Warren S. J., Leggett S. K., Hodgkin S. T., 2006, *MNRAS*, 367, 454
- Heymann F., Siebenmorgen R., 2012, *ApJ*, 751, 27
- Hodgkin S. T., Irwin M. J., Hewett P. C., Warren S. J., 2009, *MNRAS*, 394, 675
- Hönig S. F., Beckert T., Ohnaka K., Weigelt G., 2006, *A&A*, 452, 459
- Huffman D. R., 1977, *AdPhy*, 26, 129
- Iwasawa K., et al., 2012, *A&A*, 546, A84
- Jarrett T. H., et al., 2011, *ApJ*, 735, 112
- Jia J., Ptak A., Heckman T., Zakamska N., 2012, *arXiv*, [arXiv:1205.0033](https://arxiv.org/abs/1205.0033)
- Jin C., Ward M., Done C., 2012, *MNRAS*, 422, 3268
- Kauffmann G., et al., 2003, *MNRAS*, 346, 1055
- Krawczyk C. M., Richards G. T., Mehta S. S., Vogeley M. S., Gallagher S. C., Leighly K. M., Ross N. P., Schneider D. P., 2013, *ApJS*, 206, 4
- Lacy M., et al., 2004, *ApJS*, 154, 166
- Lagos C. D. P., Padilla N. D., Strauss M. A., Cora S. A., Hao L., 2011, *MNRAS*, 414, 2148
- LaMassa S. M., Heckman T. M., Ptak A., Hornschemeier A., Martins L., Sonnentrucker P., Tremonti C., 2009, *ApJ*, 705, 568
- LaMassa S. M., Heckman T. M., Ptak A., Martins L., Wild V., Sonnentrucker P., 2010, *ApJ*, 720, 786
- Lamastra A., Bianchi S., Matt G., Perola G. C., Barcons X., Carrera F. J., 2009, *A&A*, 504, 73
- Lawrence A., et al., 2007, *MNRAS*, 379, 1599
- Lusso E., et al., 2011, *A&A*, 534, A110
- Lutz D., Maiolino R., Spoon H. W. W., Moorwood A. F. M., 2004, *A&A*, 418, 465
- Magorrian J., et al., 1998, *AJ*, 115, 2285
- Mainieri V., Bergeron J., Hasinger G., Lehmann I., Rosati P., Schmidt M., Szokoly G., Della Ceca R., 2002, *A&A*, 393, 425
- Mainieri V., et al., 2011, *A&A*, 535, A80
- Maiolino R., Rieke G. H., 1995, *ApJ*, 454, 95
- Mateos S., Barcons X., Carrera F. J., Ceballos M. T., Hasinger G., Lehmann I., Fabian A. C., Streblyanska A., 2005, *A&A*, 444, 79
- Mateos S., et al., 2008, *A&A*, 492, 51
- Mateos S., et al., 2012, *MNRAS*, 426, 3271
- Nardini E., Risaliti G., Salvati M., Sani E., Watabe Y., Marconi A., Maiolino R., 2009, *MNRAS*, 399, 1373
- Nardini E., Risaliti G., Watabe Y., Salvati M., Sani E., 2010, *MNRAS*, 405, 2505
- Nenkova M., Ivezić Ž., Elitzur M., 2002, *ApJ*, 570, L9
- Nenkova M., Sirocky M. M., Ivezić Ž., Elitzur M., 2008, *ApJ*, 685, 147
- Nenkova M., Sirocky M. M., Nikutta R., Ivezić Ž., Elitzur M., 2008, *ApJ*, 685, 160
- Netzer H., Mainieri V., Rosati P., Trakhtenbrot B., 2006, *A&A*, 453, 525
- Netzer H., et al., 2007, *ApJ*, 666, 806
- Neugebauer G., Oke J. B., Becklin E. E., Matthews K., 1979, *ApJ*, 230, 79
- Pineau F.-X., Motch C., Carrera F., Della Ceca R., Derrière S., Michel L., Schwobe A., Watson M. G., 2011, *A&A*, 527, A126
- Polletta M., et al., 2007, *ApJ*, 663, 81
- Ptak A., Zakamska N. L., Strauss M. A., Krolik J. H., Heckman T. M., Schneider D. P., Brinkmann J., 2006, *ApJ*, 637, 147
- Reyes R., Zakamska N.L., Strauss M.A., et al. 2008, *AJ*, 136, 2373
- Richards G. T., et al., 2002, *AJ*, 123, 2945
- Richards G. T., et al., 2006, *ApJS*, 166, 470
- Roseboom I. G., Lawrence A., Elvis M., Petty S., Shen Y., Hao H., 2012, *MNRAS*, 406
- Salim S., et al., 2005, *ApJ*, 619, L39
- Schartmann M., Meisenheimer K., Camenzind M., Wolf S., Tristram K. R. W., Henning T., 2008, *A&A*, 482, 67
- Severgnini P., Caccianiga A., Della Ceca R., 2012, *A&A*, 542, A46
- Shi Y., Helou G., Armus L., Stierwalt S., Dale D., 2012, *arXiv:1212.3642*
- Skrutskie M. F., et al. 2006, *AJ*, 131, 1163
- Stern D., et al., 2005, *ApJ*, 631, 163
- Stern D., Assef R.J., Benford D.J., et al. 2012, *ApJ*, 753, 30
- Stoughton C., et al., 2002, *AJ*, 123, 485
- Strauss M. A., et al., 2002, *AJ*, 124, 1810
- Sturm E., Hasinger G., Lehmann I., Mainieri V., Genzel R., Lehnert M. D., Lutz D., Tacconi L. J., 2006, *ApJ*, 642, 81
- Suganuma M., et al., 2006, *ApJ*, 639, 46
- Tozzi P., et al., 2006, *A&A*, 451, 457
- Treister E., Urry C. M., Virani S., 2009, *ApJ*, 696, 110
- Tremaine, S., and 14 colleagues 2002. The Slope of the Black Hole Mass versus Velocity Dispersion Correlation. *The Astrophysical Journal* 574, 740-753.
- Trouille L., Barger A. J., 2010, *ApJ*, 722, 212
- Vanden Berk D. E., et al., 2006, *AJ*, 131, 84
- Vignali C., Alexander D. M., Gilli R., Pozzi F., 2010, *MNRAS*, 404, 48
- Villar-Martín M., Humphrey A., Martínez-Sansigre A., et al. 2008, *MNRAS*, 390, 218
- Wall J.V. & Jenkins C.R., 2008, *Practical Statistics for Astronomers*, Cambridge University Press
- Watson M. G., et al., 2009, *A&A*, 493, 339
- Worsley M. A., et al., 2005, *MNRAS*, 357, 1281
- Wright E. L., et al., 2010, *AJ*, 140, 1868
- Xue Y. Q., et al., 2011, *ApJS*, 195, 10
- Yan L., et al., 2012, *arXiv*, [arXiv:1209.2065](https://arxiv.org/abs/1209.2065)
- York D. G., et al., 2000, *AJ*, 120, 1579
- Zakamska N. L., Gómez L., Strauss M. A., Krolik J. H., 2008, *AJ*, 136, 1607